

Engineering Journal



American Institute of Steel Construction

Third Quarter 2015 Volume 52, No. 3

- 175 Evaluating Accumulation of Fatigue Damage in Steel Bridges Using Measured Strain Data
Jeremiah Fasl, Todd Helwig, Sharon L. Wood, and Karl Frank
- 185 Design of Split-Tee Connections for Special Composite Moment Frames
Erica C. Fischer and Amit H. Varma
- 203 Structural Innovation: Combining Classic Theories with New Technologies
William F. Baker, Lauren L. Beghini, Arkadiusz Mazurek, Juan Carrion and Alessandro Beghini

ENGINEERING JOURNAL

AMERICAN INSTITUTE OF STEEL CONSTRUCTION

*Dedicated to the development and improvement of steel construction,
through the interchange of ideas, experiences and data.*

Editorial Staff

Editor: MARGARET A. MATTHEW, P.E.

Managing Editor: KEITH A. GRUBB, S.E., P.E.

Research Editor: JUDY LIU, PH.D.

Production Editor: MEGAN JOHNSTON-SPENCER

Officers

JEFFREY E. DAVE, P.E., *Chairman*

Dave Steel Company, Inc., Asheville, NC

JAMES G. THOMPSON, *Vice Chairman*

Palmer Steel Supplies, Inc., McAllen, TX

ROGER E. FERCH, P.E., *President*

American Institute of Steel Construction, Chicago

DAVID B. RATTERMAN, *Secretary & General Counsel*

American Institute of Steel Construction, Chicago

CHARLES J. CARTER, S.E., P.E., PH.D., *Vice President and
Chief Structural Engineer*

American Institute of Steel Construction, Chicago

JACQUES CATTAN, *Vice President*

American Institute of Steel Construction, Chicago

JOHN P. CROSS, P.E., *Vice President*

American Institute of Steel Construction, Chicago

SCOTT L. MELNICK, *Vice President*

American Institute of Steel Construction, Chicago

The articles contained herein are not intended to represent official attitudes, recommendations or policies of the Institute. The Institute is not responsible for any statements made or opinions expressed by contributors to this Journal.

The opinions of the authors herein do not represent an official position of the Institute, and in every case the officially adopted publications of the Institute will control and supersede any suggestions or modifications contained in any articles herein.

The information presented herein is based on recognized engineering principles and is for general information only. While it is believed to be accurate, this information should not be applied to any specific application without competent professional examination and verification by a licensed professional engineer. Anyone making use of this information assumes all liability arising from such use.

Manuscripts are welcomed, but publication cannot be guaranteed. All manuscripts should be submitted in duplicate. Authors do not receive a remuneration. A "Guide for Authors" is printed on the inside back cover.

ENGINEERING JOURNAL (ISSN 0013-8029) is published quarterly. Subscriptions: Members: one subscription, \$40 per year, included in dues; Additional Member Subscriptions: \$40 per year. Non-Members U.S.: \$160 per year. Foreign (Canada and Mexico): Members \$80 per year. Non-Members \$160 per year. Published by the American Institute of Steel Construction at One East Wacker Drive, Suite 700, Chicago, IL 60601.

Periodicals postage paid at Chicago, IL and additional mailing offices. **Postmaster:** Send address changes to ENGINEERING JOURNAL in care of the American Institute of Steel Construction, One East Wacker Drive, Suite 700, Chicago, IL 60601.

Copyright 2015 by the American Institute of Steel Construction. All rights reserved. No part of this publication may be reproduced without written permission. The AISC logo is a registered trademark of AISC.

Subscribe to *Engineering Journal* by visiting our website www.aisc.org/ej or by calling 312.670.5444.

Copies of current and past *Engineering Journal* articles are available free to members online at www.aisc.org/ej.

Non-members may purchase *Engineering Journal* article downloads at the AISC Bookstore at www.aisc.org/ej for \$10 each.

Evaluating Accumulation of Fatigue Damage in Steel Bridges Using Measured Strain Data

JEREMIAH FASL, TODD HELWIG, SHARON L. WOOD, and KARL FRANK

ABSTRACT

As traffic volumes increase, bridges age, and maintenance budgets are cut, transportation officials often need quantitative data to distinguish between bridges that can be kept safely in service and those that need to be replaced or retrofitted. Strain gages can be utilized to evaluate fatigue damage in steel bridges using the techniques that are discussed in this paper. To evaluate fatigue damage, the cycles induced by vehicular traffic must be quantified using a cycle-counting algorithm, such as a rainflow algorithm. The amount of fatigue damage induced during the monitoring period can then be calculated using the traditional method, the effective stress range, or using a new approach based on the index stress range. One distinct advantage of the proposed method is that the relative amount of fatigue damage accumulated at different locations along the bridge can be easily compared. The advantages and limitations of both methods are demonstrated using measured data from a fracture-critical steel bridge.

Keywords: strain gages, fatigue measurement, steel bridges.

INTRODUCTION

Transportation officials face the difficult task of maintaining the nation's inventory of highway bridges under the pressure of reduced maintenance budgets, aging infrastructure, and increasing traffic volumes. One of the critical types of structural deterioration for steel bridges is fatigue-induced fracture. The primary method used to identify structural deterioration is hands-on visual inspections, the results of which provide transportation officials with qualitative data relative to the location and growth of cracks. However, quantitative data are often needed to distinguish between bridges that can safely remain in service and bridges that need to be replaced or retrofitted. Using the measured strain response of the bridge under service loads to evaluate the accumulation of fatigue damage is one means of providing this quantitative data.

Techniques for evaluating the accumulation of fatigue damage from measured strain data are discussed in this paper. In all cases, rainflow analyses are used to determine the spectrum of stresses at the location of each strain gage.

Potential drawbacks of using the effective stress range, which is the traditional technique used for tracking fatigue damage, are presented. The index stress range is introduced as a means of easily determining the relative accumulation of fatigue damage at multiple locations along a bridge. Techniques for visualizing fatigue damage accumulation are also presented. The measured response of a fracture-critical steel bridge is used to demonstrate the methods discussed in this paper.

BACKGROUND

Before 1970, the fatigue guidelines in the AASHTO bridge design specifications were based on the measured response of small-scale specimens that were tested under constant-amplitude loading (Schilling et al., 1978). These tests revealed that the primary variables affecting fatigue life were the stress range and configuration of the connection detail (Schilling et al., 1978). In addition, a stress range was identified, the constant-amplitude fatigue limit, S_{th} , below which the fatigue life was expected to be infinite. These concepts serve as the basis for the $S-N$ curves (Figure 1) used in the current bridge design specifications in the United States (AASHTO, 2010).

According to the AASHTO Load and Resistance Bridge Design (LRFD) Specifications (2010), for a given constant-amplitude stress range, S_r , that exceeds the constant-amplitude fatigue limit, the number of cycles to failure, N_f , can be calculated using Equation 1:

$$N_f = \frac{A}{S_r^3} \quad (1)$$

where A is the fatigue constant for the detail category defined

Jeremiah Fasl, Associate III, Wiss, Janney, Elstner Associates Inc., Austin, TX (corresponding). Email: jfasl@wje.com

Todd Helwig, Associate Professor, University of Texas–Austin. Email: thelwig@mail.utexas.edu

Sharon L. Wood, Interim Dean, Cockrell School of Engineering, University of Texas–Austin. Email: swood@utexas.edu

Karl Frank, Chief Engineer, Hirschfeld Industries. Email: karl.frank@hirschfeld.com

by AASHTO (2010). Equation 1 is used for the design of new bridges; therefore, the fatigue constant for each detail category corresponds to a low probability of failure.

Although fatigue tests have traditionally been conducted using a constant-amplitude stress range, highway bridges are subjected to stress cycles with varying amplitudes under service loads. A cumulative damage theory is used to calculate the effective stress range for a given spectrum of variable-amplitude stress cycles. The most common damage theory is Palmgren-Miner's rule (ASCE, 1982), which is based on a linear damage hypothesis. The Palmgren-Miner rule for linear damage accumulation is simple to use, and the results agree with experimental data (ASCE, 1982). Nonlinear cumulative damage theories have been proposed (i.e., Li, Chan and Ko, 2001); however, the equations are more complicated to use and the results are not consistently better than a linear damage model (ASCE, 1982).

For a connection detail subjected to constant-amplitude stress cycles, the accumulated damage ratio, D , represents the portion of the design life that has been consumed by the imposed loading cycles:

$$D = \frac{n}{N_f} \quad (2)$$

where n is the number of imposed loading cycles. For a variable-amplitude stress spectrum, the accumulated damage ratio is the sum of the fatigue damage induced by each stress range within the spectrum:

$$D = \sum_{j=1}^k \frac{n_j}{N_{fj}} \quad (3)$$

where n_j is the number of cycles imposed with a stress range of S_{rj} , N_{fj} is the number of cycles corresponding to failure at a stress range of S_{rj} and k is the number of distinct stress ranges included within the stress spectrum. If Equation 1 is

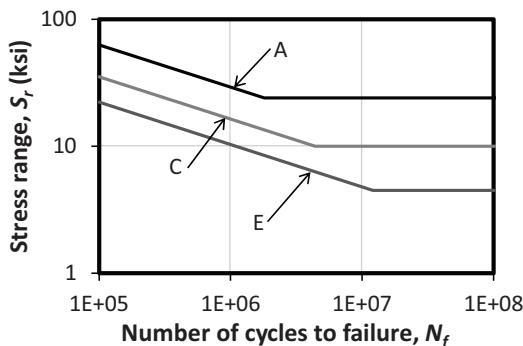


Fig. 1. Representative S-N design relationships from AASHTO (2010).

substituted into Equation 3, the damage accumulation ratio can be expressed in terms of the number of cycles imposed in each stress range, n_j , and the cube of the individual stress ranges, S_{rj} :

$$D = \sum_{j=1}^k \frac{n_j \times S_{rj}^3}{A} \quad (4)$$

Note that the damage accumulation ratio is tied to the design value of the fatigue life, rather than to the median fatigue life, for a given connection detail.

As indicated in Figure 1, the design S-N relationships are typically shown as log-log plots. If the damage accumulation ratio is included in the same graph, lines corresponding to constant values of D are parallel to the descending branch of the S-N relationship (Figure 2). Therefore, the damage accumulation ratio can be considered the portion of the design fatigue life that has been consumed during the monitoring period of the bridge.

In the previous discussion, it was assumed that the components of the stress spectrum were known. However, when using measured strain data to evaluate the fatigue response of a bridge, a cycle-counting algorithm must be used to transform the strain history into a stress spectrum, which is expressed in terms of a histogram of stress amplitudes. The simplified rainflow method outlined by Downing and Socie (1982) and included in ASTM E1049 (2011) was used for all analyses discussed in this paper. The method is well suited for fatigue analysis because it counts cycles based on closed hysteresis loops (Dowling, 1972).

Schilling and colleagues (1978) introduced the concept of an effective stress range for characterizing the fatigue resistance of connection details subjected to variable-amplitude loading. The fatigue damage induced by a spectrum of stress cycles is the same as the fatigue damage induced by the total number of stress cycles within the spectrum, n_m , at the effective stress range, S_{re} :

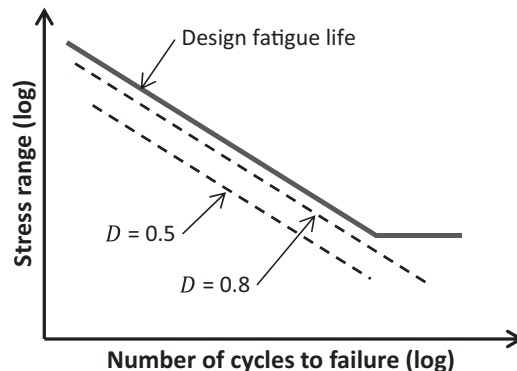


Fig. 2. Different levels of the damage accumulation ratio superimposed on S-N relationship used for design.

$$D = \frac{n_m \times S_{re}^3}{A} \quad (5)$$

Setting Equation 5 equal to Equation 4 leads to the definition of the effective stress range:

$$S_{re} = \left(\sum_{j=1}^k \frac{n_j}{n_m} S_{rj}^3 \right)^{1/3} \quad (6)$$

The relationship between the total number of stress cycles, n_m , the effective stress range, S_{re} , and the damage accumulation ratio, D , is illustrated in Figure 3. The total number of stress cycles within the stress spectrum is calculated using the rainflow counting algorithm to evaluate the measured strain history. The damage accumulation ratio is calculated from the stress spectrum using Equation 5. The effective stress range can also be calculated from the stress spectrum using Equation 6.

The effective stress range is an efficient method to relate the cycles from a spectrum of stress ranges to a single, equivalent stress range. The single, equivalent stress range is a useful metric because it can be used to calculate the remaining fatigue life, as discussed in Fasl (2013). One of the limitations of this traditional approach for evaluating the accumulation of fatigue damage from measured strain data is that both the effective stress range and the total number of cycles during the monitoring period must be used to characterize the extent of fatigue damage at a given location. Nonetheless, both of these parameters vary with location along the bridge, which complicates comparison of fatigue data from multiple sensors using the effective stress range as the sole parameter.

To illustrate that limitation, the effective stress range and number of cycles for three representative gage locations are

presented (Figure 4). Because both the effective stress range and number of cycles are larger for gage b than for gage a, it is obvious that gage b has a higher accumulation of damage than gage a. Likewise, because the number of cycles for gage c is larger than gage a, while the effective stress ranges are equal, gage c has a higher accumulation of damage than gage a. Nonetheless, comparing the relative accumulation of damage between gages b and c is more complicated. Gage b has a higher effective stress range but a fewer number of cycles than gage c. Using the historical method of evaluating fatigue, the only way to compare the two gage locations would be to calculate the remaining fatigue life or plot the damage accumulation ratio (Figure 4). A new approach, the index stress range, which is introduced later in this paper, was developed to quantify the relative accumulation of damage between gages.

Data from a fracture-critical steel bridge that was monitored for nearly a year by the research team were used in this paper to highlight the advantages of using the index stress range to evaluate the accumulation of fatigue data.

DESCRIPTION OF BRIDGE

The strain response of a fracture-critical steel bridge with significant truck traffic was monitored as part of this investigation. The average daily truck traffic was reported as 4,000 trucks per day, with nearly 60 percent of those trucks featuring five or more axles. The bridge was constructed in 1935 and comprises three spans (73.5-ft end spans and a 125-ft center span) for a total length of 272 ft (Figure 5). The longitudinal girders in the end spans are continuous over the interior supports and extend 30.5 ft into the center span. The bridge is statically determinate, and the center section is suspended by hangers between the overhangs within the middle span. The bridge is considered to be fracture critical

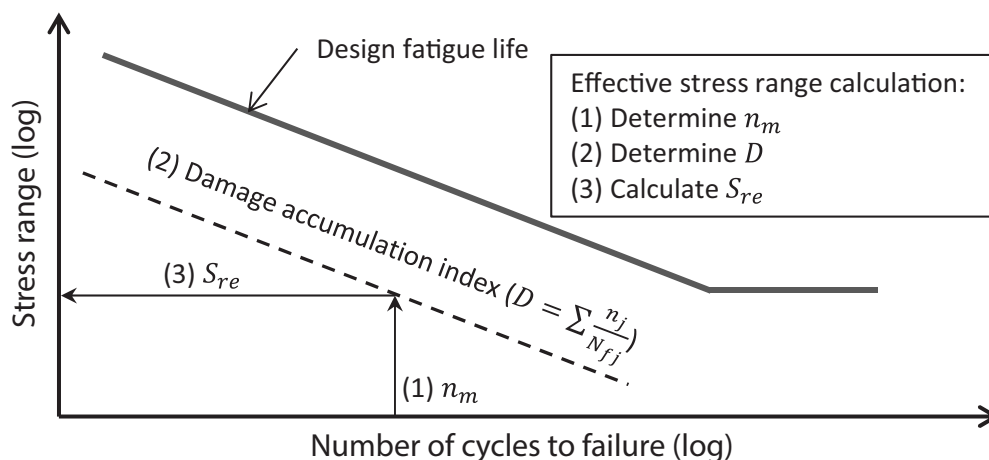


Fig. 3. Graphical representation of the method used to determine the effective stress range for a given stress spectrum.

because the superstructure includes only two longitudinal girders and the failure of a flange from one girder would be expected to lead to the collapse of the entire bridge.

The longitudinal girders are built-up sections (Figure 6) that are spaced 23 ft apart (center-to-center). The girders are haunched, with a girder depth of 8 ft over the interior piers, 5 ft at midspan of the bridge and 5.54 ft at the end supports. Double angles serve as the flanges of the built-up section and were riveted to the web plate. Cover plates were riveted to the flanges near the interior supports and at the

center of the suspended span to increase the moment capacity. Transverse floor beams provide lateral support for the longitudinal girders and are spaced 7.5 ft on-center along the length of the bridge. The webs of the floor beams are riveted to angles that serve as stiffeners for the longitudinal girders. Traffic originally traveled in both the southbound and northbound directions.

In 1974, the deck of the bridge was widened and welds were added to connect the top flange of the longitudinal girders to the top flange of the floor beams and to the top flange of the brackets that support the overhang (Figure 6). A plan view of the detail is presented in Figure 7. The widened deck was not made composite with the longitudinal girders. When the bridge was widened, a separate bridge was added for southbound traffic; therefore, traffic currently crosses the bridge in the northbound direction of the two-lane steel bridge. Accordingly, over the entire life of the bridge, the majority of the trucks are expected to cross the bridge in the right lane, which is supported by the east girder.

The welds that were added for the bridge widening correspond to a category E detail (AASHTO, 2010). Reports from recent inspections conducted by the bridge owner indicated that cracks had formed and were growing at the welded connections between the longitudinal girders and floor beams at locations where the cover plates were not present (Figure 8). Although the live load moments were calculated to

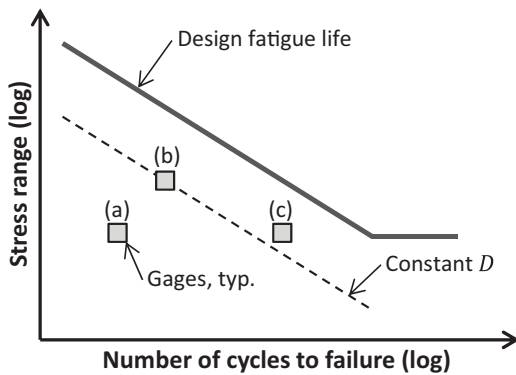


Fig. 4. Comparison of relative damage levels for three gage locations.

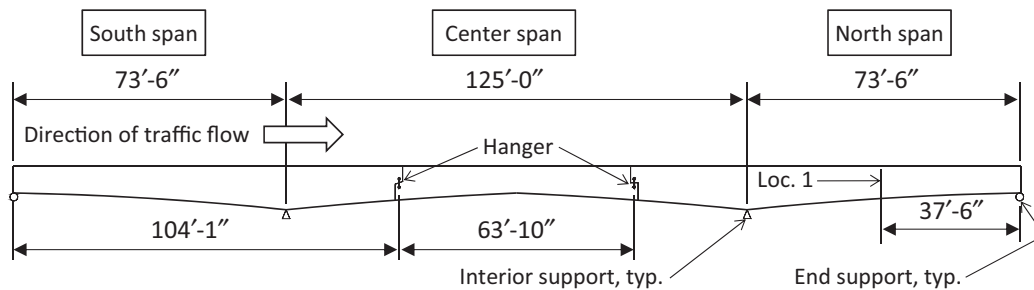


Fig. 5. Elevation of the bridge and location of strain gages.

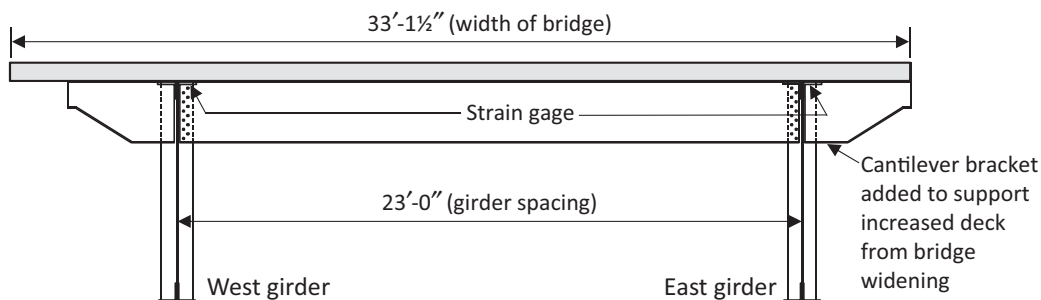


Fig. 6. Cross-section of the bridge (looking north).

be greater at the interior supports, the flexural stresses in the longitudinal girders were calculated to be greater at the locations of the observed cracks because the moment of inertia was less.

Strain gages were installed on both the top and bottom flanges of the longitudinal girders at several locations along the length of the bridge. The complete set of strain data is presented in Fasl (2013). In this paper, only data collected from strain gages installed on the top flange of each longitudinal girder (Figure 6) at location 1 near the north support (Figure 5) are presented. To monitor the live load response of the longitudinal girder, the strain gages were installed 2 ft south of the connection between the stiffener angles and the floor beams/brackets.

At the location of the strain gages, negative moment is induced when a vehicle is in the center span and positive moment is induced when a vehicle is in the north span. The difference in strain readings between the maximum positive and maximum negative readings determines the maximum stress range for a given vehicle crossing the bridge.

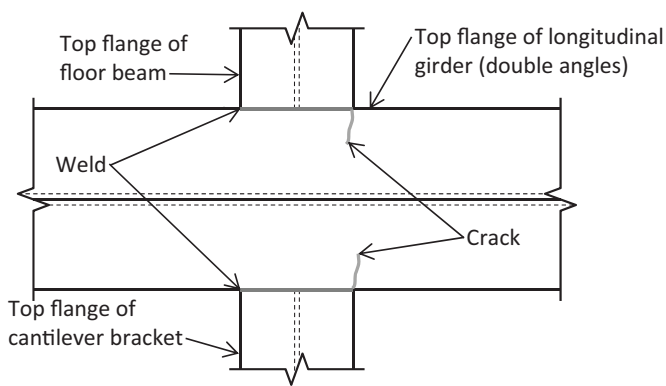


Fig. 7. Plan view of category E detail.

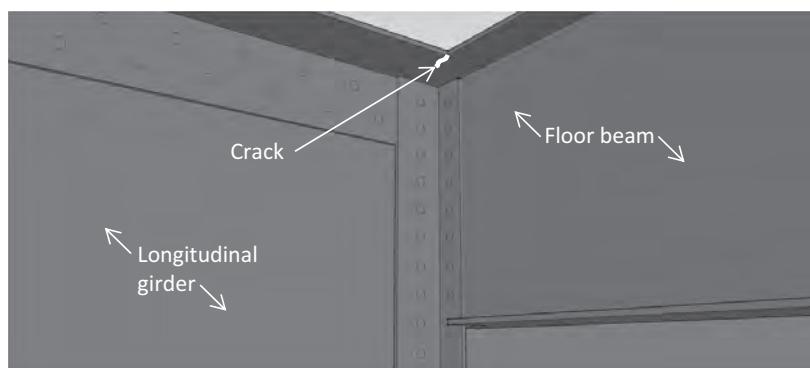


Fig. 8. Three-dimensional schematic of crack at weld between the floor beam and longitudinal girder.

MEASURED RESPONSE OF BRIDGE

The research team collected strain data for 71 days at an effective scan rate of 50 Hz. Strain histories were analyzed in 30-min segments to minimize the errors associated with temperature drift (Fasl et al., 2010). A minimum cycle amplitude of 2 microstrain (0.06 ksi) was used when processing the data to avoid counting cycles attributed to electromechanical noise within the data acquisition system. Strains were converted to stresses using Hooke's law and a modulus of elasticity for steel of 29,000 ksi.

The resulting histograms corresponding to the stress spectra are shown in Figure 9. Two hundred bins were used in the rainflow analyses; each bin was 5 microstrain (0.15 ksi) wide. The data are presented in terms of the average number of cycles per day to facilitate comparisons with other bridges. Each gage experienced several extremely large-amplitude stress cycles (>15 ksi) during the 71-day monitoring period.

The bridge was expected to have a finite fatigue life because a large portion of the cycles in the stress spectra for each girder exceeded the constant amplitude fatigue limit for category E details (4.5 ksi). This assumption was confirmed by the rate of crack growth observed at several of the welded connections (Fasl, 2013).

For this bridge, evaluation of the accumulated fatigue damage at the locations of the two strain gages was straightforward. The stress spectrum for the east girder included an average of 56,000 cycles/day with an effective stress range of 2.26 ksi. In contrast, the stress spectrum for the west girder included an average of 38,000 cycles/day with an effective stress range of 1.44 ksi. Because both the effective stress range and the number of cycles were greater for the east girder, the east girder accumulated more fatigue damage than the west girder during the monitoring period. This observation was expected because traffic currently crosses the bridge only in the northbound direction and the east girder is below the right lane of traffic; therefore, the

volume of truck traffic is expected to be higher in the right lane rather than the left lane. However, the relative accumulation rates of fatigue damage in the two girders are not readily apparent from the results of this analysis.

INDEX STRESS RANGE

The index stress range method was proposed by Fasl and colleagues (2012) as a means of expressing the fatigue damage accumulation in terms of a single parameter. This method facilitates comparisons among multiple strain gages positioned along the same bridge and can also be used to compare the accumulation rate of fatigue damage among bridges within an inventory of bridges.

The method is summarized in Figure 10. As a first step, the engineer selects the value of the index stress range, \hat{S}_{ri} , to be used in the calculations. Although the choice is arbitrary, the constant-amplitude fatigue limit, S_{th} , is a convenient choice. Then the effective number of cycles at the index stress range, \hat{n}_i , is calculated such that the accumulated

fatigue damage induced is the same as that induced by the measured stress spectrum:

$$D = \sum_{j=1}^k \frac{n_j \times S_{rj}^3}{A} = \frac{\hat{n}_i \times \hat{S}_{ri}^3}{A} \quad (7)$$

The effective number of cycles at the index stress range can be calculated by rearranging the terms in Equation 7:

$$\hat{n}_i (\hat{S}_{ri}) = \sum_{j=1}^k \frac{n_j \times S_{rj}^3}{\hat{S}_{ri}^3} \quad (8)$$

For the stress spectra shown in Figure 9, and an index stress range equal to S_{th} [4.5 ksi for category E details (AASHTO, 2010)], the east girder experienced an average of 7,100 equivalent stress cycles a day compared with an average of 1,250 equivalent stress cycles a day for the west girder. The advantage of the method is that the relative amount of damage can be determined directly because the data are normalized to the same stress range. For instance,

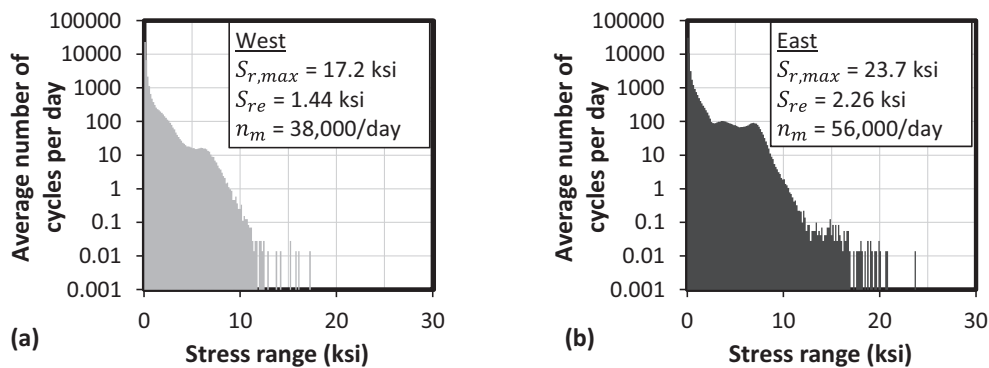


Fig. 9. Stress spectra calculated from the strain histories recorded from the top flange of the (a) west girder and (b) east girder.

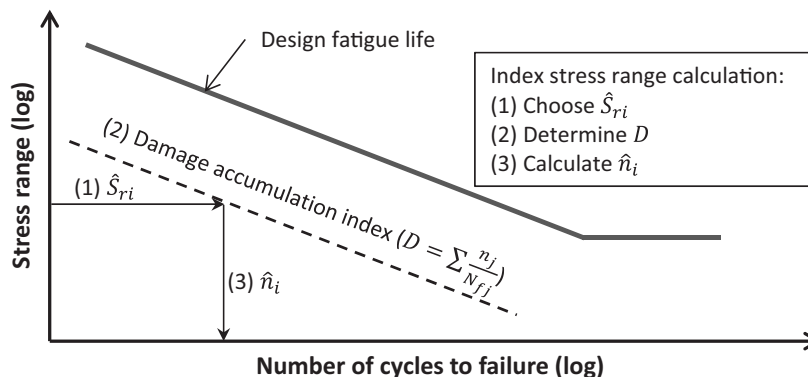


Fig. 10. Graphical representation of the method used to determine the effective number of cycles at the index stress range for a given stress spectrum.

at this bridge, the east girder accumulated 5.5 (7,100/1,250) times as much damage as the west girder during the monitoring period.

If a different value had been selected for the index stress range, the number of equivalent stress cycles would be different, but the fatigue damage accumulation ratio for each girder would remain unchanged. Therefore, direct comparisons of the relative amount of fatigue damage are always possible.

VISUALIZATION OF FATIGUE DAMAGE

The advantages of the index stress method extend beyond the direct means of comparing the accumulation of fatigue damage from different stress spectra. The index stress method also provides a means of visualizing the impact of decisions made during the processing of raw strain data.

One concern associated with using the Palmgren-Miner rule with stress spectra corresponding to measured strain data is the influence of low-amplitude stress cycles (Fisher, Kulak and Smith, 1998). When tested in the laboratory using constant-amplitude stress cycles, connection details exhibited an infinite fatigue life when the amplitude of the applied stress cycles was less than S_{th} . However, for variable-amplitude fatigue, there is not agreement on the influence of cycles with stress ranges below S_{th} . Swenson and Frank (1984) showed that all cycles contribute to the accumulation of fatigue damage, while Connor and Fisher (2006) recommended truncating cycles with amplitudes less than 25 to 50% of S_{th} from the measured stress spectrum.

Despite the lack of consensus, many engineers truncate data without analyzing the impact of all cycles on the accumulation of fatigue damage. As such, new visualization techniques were developed and are discussed herein to allow an engineer to assess the influence of all stress ranges to the accumulation of fatigue damage.

If traditional approaches are used to characterize the accumulated fatigue damage, both the effective stress range

and the number of cycles vary as the lower amplitude cycles are truncated from the stress spectrum. Data from the east longitudinal girder are plotted in Figure 11. The horizontal axis corresponds to the ratio of the minimum stress range retained in the stress spectrum, $S_{r,min}$, to the constant-amplitude fatigue limit, S_{th} .

Because a large number of low-amplitude cycles are included in the stress spectrum (Figure 9b), the number of cycles included in the calculations decreased rapidly as the lower-amplitude cycles were truncated from the spectrum. If all cycles less than $0.1S_{th}$ were truncated, the total number of cycles within the stress spectrum decreased by more than 80%. In contrast, the effective stress range increased by more than 100% if all cycles less than $0.2S_{th}$ were truncated. These changes in n_m and S_{re} imply that the accumulated fatigue damage is extremely sensitive to the value of $S_{r,min}$ used in the calculations. However, the damage accumulation ratio, D , decreased by less than 5% when $S_{r,min}$ was taken as $0.5S_{th}$. This example highlights the interactions between S_{re} and n_m and demonstrates that using only the effective stress range to characterize the accumulated fatigue damage is misleading.

In contrast, the effective number of cycles at the index stress level, \hat{n}_i , provides a clear interpretation of the relationship between the accumulated fatigue damage and $S_{r,min}$ (Figure 12). In this case, a single parameter is sufficient to characterize the accumulation of fatigue damage.

The previous discussion focused on the influence of low-amplitude stress cycles on the accumulation of fatigue damage. The techniques discussed in this paper can also be used to identify the stress ranges within a measured spectrum that have the largest influence on the fatigue damage accumulation. When utilizing stress spectra acquired in the field, engineers are typically concerned whether the lower and higher stress ranges are load induced or are due to limitations of the data acquisition system. Electromechanical noise in the data acquisition equipment can cause fictitious low-amplitude cycles, whereas lightning strikes or CB

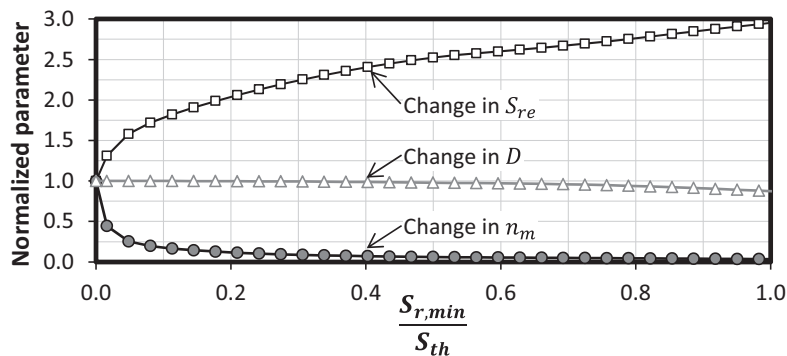


Fig. 11. Sensitivity of effective stress range and number of cycles to the minimum stress range retained in the stress spectrum for the east girder.

radios can cause large-amplitude spikes. The contribution of the stress cycles within each bin of the stress spectrum (Figure 9) can be evaluated using Equation 9.

$$D_j = \frac{n_j \times S_{rj}^3}{A} \quad (9)$$

where D_j is the portion of the damage accumulation ratio attributable to bin j and S_{rj} is the average stress for the cycles grouped in bin j . The data for the east and west girders are plotted in Figure 13 and provide additional evidence that the fatigue damage accumulated much more rapidly in the east girder than the west girder. The plot also provides evidence that the extremely large amplitude stress cycles (greater than 15 ksi) did not influence the accumulation of fatigue damage because the number of those cycles was so low. Stress cycles with amplitudes of approximately 7.5 ksi had the highest influence on the east girder, while stress cycles with amplitudes of approximately 6.5 ksi had the highest influence on the west girder.

The same data can be plotted in terms of the cumulative fatigue damage in order to better understand the impact of stress ranges within the stress spectrum. The cumulative

fatigue data are normalized in Figure 14 by dividing the data from each girder by ΣD_j , which represents the total fatigue damage induced during the 71-day monitoring period. The differences in the rates of fatigue damage accumulation between the two girders cannot be detected from the normalized data, but approximately 95% of the fatigue damage in the east girder was induced by stress cycles between 1 and 9 ksi, while approximately 95% of the fatigue damage in the west girder was induced by stress cycles between 2 to 10 ksi. For this bridge, it did not matter if the lower bins were truncated or considered in the analysis because cycles below 1 ksi contributed less than 2.5% to the total damage. The damage at the site is dominated by typical truck traffic, whereas cycles greater than 10 ksi only contributed approximately 2.5% of the damage.

CONCLUSIONS

Using the procedures described in this paper, the amount of fatigue damage can be determined and characterized. The index stress range provides a method for assessing the relative damage accumulation between gage locations and/or bridges. Because the damage is normalized using the

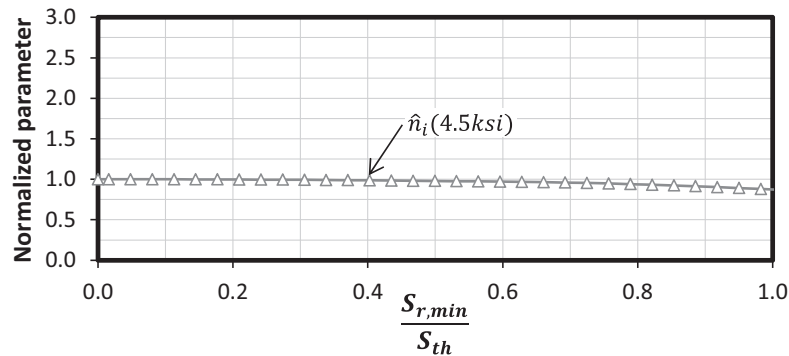


Fig. 12. Sensitivity of effective number of cycles at the index stress range to the minimum stress range retained in the stress spectrum for the east girder.

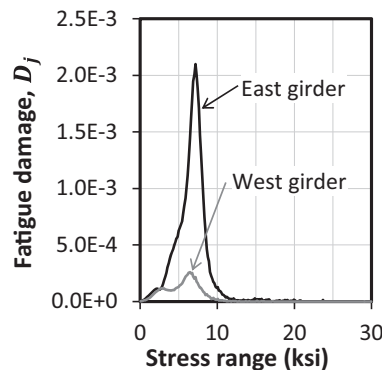


Fig. 13. Contribution of each bin to the total fatigue damage accumulated during the monitoring period.

method, the number of cycles at the index stress range is a better indicator of damage. The method can also be used to calculate the contribution of damage from each stress range. Because both low-amplitude (electromechanical noise) and high-amplitude (electromechanical spikes within the data acquisition system) stress ranges are questioned during a monitoring program, the impact of all stress ranges can be evaluated using the visualization techniques. If the cycles are contributing more to the damage than expected, those cycles can be analyzed further. Engineers can use judgment on how to handle cycles below the constant-amplitude fatigue limit, S_{th} , in the absence of international agreement. However, the lower cycles may not significantly contribute to fatigue damage (as demonstrated using the data from the fracture-critical steel bridge monitored by the research team).

ACKNOWLEDGMENTS

This research was funded by the National Institute of Standards and Technology (NIST) through the Technology Innovation Program (TIP). The opinions expressed in this paper are those of the researchers and do not necessarily represent those of the sponsor. The researchers would like to thank the bridge owner for providing access to the bridge. In addition, Vasilis Samaras, Matt Reichenbach and Ali Abu Yosef made significant contributions to the research project.

SYMBOLS

A Fatigue constant used in AASHTO (2010) design specifications to calculate fatigue life for a given detail category

- D Accumulated damage ratio
- D_j Portion of accumulated damage ratio corresponding to bin j of a stress spectrum
- N_f Number of cycles to failure for a given constant-amplitude stress range, S_r , calculated using AASHTO (2010) design specifications
- N_{fj} Number of cycles to failure for stress range S_{rj} , calculated using AASHTO (2010) design specifications
- S_r Constant-amplitude stress range
- S_{re} Effective stress range
- \hat{S}_{ri} Index stress range
- S_{rj} Average stress range within bin j of a stress spectrum
- $S_{r,min}$ Minimum stress range retained in a measured stress spectrum
- S_{th} Constant-amplitude fatigue limit defined in AASHTO (2010)
- k Number of distinct stress ranges included within a stress spectrum
- n Number of loading cycles imposed at a constant-amplitude stress range, S_r
- n_j Number of loading cycles imposed at a stress range S_{rj} within a stress spectrum
- \hat{n}_i Effective number of loading cycles at the index stress range, \hat{S}_{ri} , for a given stress spectrum
- n_m Total number of measured stress ranges with a stress spectrum

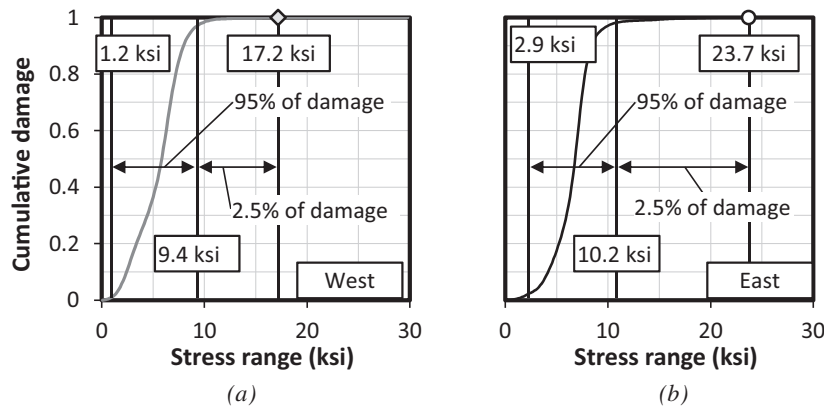


Fig. 14. Normalized cumulative damage during the monitoring period for the west (a) and east (b) girders.

REFERENCES

- AASHTO (2010), AASHTO LRFD Bridge Design Specifications, American Association of State Highway and Transportation Officials, Washington, DC.
- ASCE Committee on Fatigue and Fracture Reliability (1982), "Fatigue Reliability: Variable Amplitude Loading," *Journal of the Structural Division*, ASCE, Vol. 108, No. ST1, pp. 47–69.
- ASTM (2011), Standard Practices for Cycle Counting in Fatigue Analysis, E1049-85, ASTM International, West Conshohocken, PA.
- Connor, R. and Fisher, J. (2006), "Identifying Effective and Ineffective Retrofits for Distortion Fatigue Cracking in Steel Bridges Using Field Instrumentation," *Journal of Bridge Engineering*, Vol. 11, No. 6, pp. 745–752.
- Dowling, N. (1972), "Fatigue Failure Predictions for Complicated Stress-Strain Histories," *Journal of Materials*, Vol. 7, No. 1, pp. 71–87.
- Downing, S. and Sqcic, D. (1982), "Simple Rainflow Counting Algorithms," *International Journal of Fatigue*, Vol. 4, No. 1, pp. 31–40.
- Fasl, J. (2013), "Evaluating the Remaining Fatigue Life of Steel Bridges Using Field Measurements," PhD Dissertation, The University of Texas at Austin.
- Fasl, J., Helwig, T., Wood, S. L., Samaras, V., Yousef, A., Frank, K., Potter, D. and Lindenberg, R. (2010), "Development of Rapid, Reliable, and Economical Methods for Inspection and Monitoring of Highway Bridges," *Proc., IABMAS 2010*, Taylor & Francis, Philadelphia, PA.
- Fasl, J., Helwig, T., Wood, S. L. and Frank, F. (2012), "Using Strain Data to Estimate the Remaining Fatigue Life of a Fracture-Critical Bridge," *Transportation Research Record*, No. 2313, pp. 63–71.
- Fisher, J., Kulak, G. and Smith, I. (1998), "A Fatigue Primer for Structural Engineers," National Steel Bridge Alliance, Chicago, IL.
- Li, Z., Chan, T. and Ko, K. (2001), "Fatigue Analysis and Life Prediction of Bridges with Structural Health Monitoring Data—Part I: Methodology and Strategy," *International Journal of Fatigue*, Vol. 23, pp. 45–53.
- Schilling, C., Klippstein, K., Barsom, J. and Blake, G. (1978), "Fatigue of Welded Steel Bridge Members Under Variable-Amplitude Loadings," NCHRP Report 188, Transportation Research Board, Washington, DC.
- Swenson, K. and Frank, K. (1984), "The Application of Cumulative Damage Fatigue Theory to Highway Bridge Fatigue Design," FHWA/TX-86/07+306-2F, Center for Transportation Research, Austin, TX.

Design of Split-Tee Connections for Special Composite Moment Frames

ERICA C. FISCHER and AMIT H. VARMA

ABSTRACT

The beam-to-column connections of special composite moment frames (C-SMFs) serving as the primary seismic force resisting system (SFRS) of a building structure are required to meet the performance criteria specified in the 2010 AISC *Seismic Provisions*. Chapter K of the *Seismic Provisions* states that experimental results should be used to provide evidence that the specific beam-to-column connection satisfies the requirements for strength and story-drift angle. This paper focuses on the split-tee connection for C-SMFs with wide flange (WF) beams and rectangular concrete-filled tube (CFT) columns. The paper provides a general description of the split-tee connection identifying its key features and components. This is followed by discussion of expected behavior in the elastic and inelastic ranges of cyclic loading. This discussion is based on prior research and large-scale testing, and it focuses on the various limit states controlling the strength and deformation capacity of the connection. The paper includes the complete design procedure for split-tee connections along with a detailed design example. The information presented in this paper can be used to create a body of evidence to apply for prequalification of similar split-tee connections in C-SMFs.

Keywords: seismic design, special composite moment frames, moment connection, composite construction, prequalification.

INTRODUCTION

The AISC *Seismic Provisions* (AISC, 2010a) provide design requirements and performance criteria for beam-to-column connections in moment frames that serve as the primary seismic force resisting systems (SFRSs) for steel building structures. The AISC *Prequalified Connections* (AISC, 2010b), however, does not include examples of beam-to-column connections for composite moment frame construction. The engineer is required to (1) present experimental results for the desired beam-to-column connection configuration and (2) demonstrate that the connection meets the performance requirements set forth in the AISC *Seismic Provisions*. This paper provides an overview of previous research performed on split-tee connections for special composite moment frames (C-SMFs) and highlights potential failure modes of the connection. It also includes comprehensive guidance and a complete example for the design and detailing of split-tee connections in C-SMFs. The connection is detailed to achieve the strength and story-drift angle requirements of the AISC *Seismic Provisions*.

This paper, along with the results of the test results from Peng (2001), provides the tools required for structural engineers to create a body of evidence to apply for prequalification of similar split-tee connections in C-SMFs. The testing requirements outlined in Section K2 of the AISC *Seismic Provisions* are satisfied by the experimental program discussed here and in detail by Peng. This paper includes a comprehensive design procedure that satisfies the requirements of Section K1.5 of the AISC *Seismic Provisions*. It also outlines many of the necessary sections of the “Prequalification Record” required by Section K1.6 of the AISC *Seismic Provisions*, including the following:

- A general description of the prequalified connection.
- A description of expected behavior of the connection in the elastic and inelastic ranges.
- A definition of the region of connection that comprises the protected zone.
- A detailed description of the design procedure for the connection.
- A list of references of test reports, research reports and other publications that provide a basis for prequalification.

Erica C. Fischer, P.E., Ph.D. Candidate, Lyles School of Civil Engineering, Purdue University, West Lafayette, IN (corresponding author). Email: fischere@purdue.edu

Amit H. Varma, Ph.D., Professor, Lyles School of Civil Engineering, Purdue University, West Lafayette, IN. Email: ahvarma@purdue.edu

Paper No. 2013-29R

BACKGROUND

Composite construction originated in Chicago in the late 1800s and is currently being used around the world in a variety of applications. Examples of buildings with composite

construction for seismic resistance include the Two Union Square in Seattle, Washington, and the Jinyuan Building in Xiamen, Fujian, China. Composite construction optimizes the contributions of steel and concrete materials and provides members that are structurally efficient in terms of stiffness, strength and self-weight (Varma et al., 2002). In concrete-filled tube (CFT) columns, the concrete restrains the steel tube flanges from local buckling inward, and the steel tube confines the concrete infill (Lai, Varma and Zhang, 2014). The steel tube also acts as formwork for placing the concrete during construction. CFT columns and frames have been used in different building structures around the world; however, this paper focuses on their use as C-SMF construction for seismic design.

Section G3 of the AISC *Seismic Provisions* provides the design basis for C-SMFs. C-SMFs are expected to develop their seismic performance through inelastic deformations in the beams, column bases and limited yielding in the column panel zones. The beam-to-column connections are required to (1) satisfy the story-drift angle requirement of 0.04 rad, (2) develop at least 80% of the nominal plastic moment capacity of the beam at 0.04-rad drift and (3) develop the required shear strength of the connection. The required shear strength is based on the load combinations that include the amplified seismic load, E_{mh} , calculated using Equation 1 (AISC-341 Equation G3-3):

$$E_{mh} = 2 \left[\frac{1.1M_{p,exp}}{L_h} \right] \quad (1)$$

where, $M_{p,exp}$ is the expected plastic moment capacity of the beam and L_h is the distance between the plastic hinge locations in the beam.

The AISC *Seismic Provisions* require the beam-to-column connections in composite moment frames to engage both the steel and concrete portions of the column and thus transfer forces effectively during a seismic event. This can be achieved through direct bearing from internal bearing mechanisms, shear connections, shear friction or a combination of these means (Peng, 2001).

AISC SEISMIC PROVISIONS

Section G3.6b of the 2010 AISC *Seismic Provisions* requires the beam-to-column connections of C-SMFs to satisfy the following:

1. The connection shall be capable of accommodating a story-drift angle of at least 0.04 rad.
2. The measured flexural resistance of the connection, determined at the column face, shall equal at least $0.8M_p$ of the connected beam at a story-drift angle of 0.04 rad, where M_p is nominal plastic moment capacity of the beam.

Typical beam-to-column connections used in C-SMFs can be categorized as beam uninterrupted or beam interrupted connections. Beam uninterrupted connections consist of beams that are continuous through the composite column; beam flange welded joints are not used, and the connection is not susceptible to premature fracture. Beam uninterrupted connections were tested by Schneider and Alostaz (1998) and others, and they demonstrated good ductility when subjected to cyclic loading. Beam interrupted connections consist of beams that are interrupted at the composite column faces and connected to them using welded or bolted connections.

There are no prequalified beam-to-column connections for C-SMFs. As a result, beam-to-column connections in C-SMFs must satisfy requirements 1 and 2 listed earlier in accordance with Chapter K of the AISC *Seismic Provisions*. Chapter K provides guidelines for using experimental results from large-scale beam-to-column connection tests to satisfy both the requirements. For beam uninterrupted connections, the AISC *Seismic Provisions* require testing results in accordance with Section K2 but also permit other substantiating data in the literature (e.g., Kanno and Deierlein, 1997). For beam interrupted connections, the AISC *Seismic Provisions* require testing results to be submitted in accordance with Section K2. Minimums of two tests are required with the same or very similar beam and column sizes as those designed for in the building structure.

SPLIT-TEE CONNECTION

AISC *Seismic Provisions* require fully restrained (FR) connections to be used in C-SMF systems. FR connections have the capacity to deform elastically as the structure deflects and story drift increases. This deformation redistributes the moment from the beam to the column as a plastic hinge forms in the C-SMF beams. The split-tee connection is an example of an FR connection with interrupted beams. A schematic of the split-tee connection is shown in Figure 1.

As shown in Figure 1, the (interrupted) wide-flange (WF) beams—the C-SMF beams—are connected to the composite CFT columns with split-tee moment connections. These connections utilize pretensioned through bolts to attach the split-tee flanges to the column. These bolts pass through holes cast into the concrete infill and are pretensioned to the CFT columns. Figure 1a shows a bolted split-tee connection where the split-tees are also bolted to the beam flanges. Figure 1b shows a bolted-welded split-tee connection where the split-tees are welded to the beam flanges. As shown, the connection length may be longer for the all-bolted split-tee connection. Shear studs are used within the CFT column to engage the concrete infill. Figures 1a and 1b show the pretensioned through bolts and shear studs.

The split-tee connection is designed so that seismic loading causes plastic hinges in the WF steel beams outside of

the connection region. The plastic hinge zones extend from the face of the column to one-half the beam depth beyond the plastic hinge point and are considered protected zones. The expected plastic moment, $M_{p,exp}$, in the beam hinges is resolved into effective forces, $M_{p,exp}/d$, in the beam flanges. These forces are transferred to the stems of the split-tees using bolts in Figure 1a and welds in Figure 1b. The shear force associated with the plastic mechanism in the frame and the gravity loads is transferred to the column through the split-tee stems as well. The split-tee is pretensioned to the CFT column, and the pretensioning is designed to resist the beam flange force without decompression and to transfer the shear force through friction between the column faces and the split-tee flanges. The panel-zone shear in the CFT column is resisted primarily by the webs of the steel tube and the compression strut in the concrete infill. Figure 2 illustrates this force transfer mechanism for the split-tee connection.

The experimental data presented in detail by Peng (2001) and summarized by Ricles, Peng and Lu (2004) shows that beam-column subassemblies with split-tee connections

exhibit ductile behavior under cyclic loading. Relative rotation between the wide-flange beams and CFT column is calculated as the sum of (1) beam rotation, (2) column rotation, (3) panel-zone shear deformation and (4) connection deformation. For the all-bolted split-tee connection shown in Figure 1a, the relative rotation is larger due to slip between the split-tee and WF beam flange and the flexibility of the split-tee itself. The relative rotation of split-tee connections can be reduced by welding the split-tee to the WF beam flange, which eliminates the slip between them. This detail, shown in Figure 1b, will also eliminate pinching in cyclic (hysteresis) response, which was observed in the all-bolted split-tee connections. As discussed in Ricles, Peng and Lu, this pinching was primarily due to the elongation of bolt holes during large story drifts.

As shown in Figure 1a, through bolts and shear studs are used in split-tee connections to engage both the steel and concrete portions of CFT columns in C-SMFs. This allows for a concrete compression strut to form in the panel zone of the CFT column with minimal yielding of the steel tube. This was observed in the tests performed by Peng (2001).

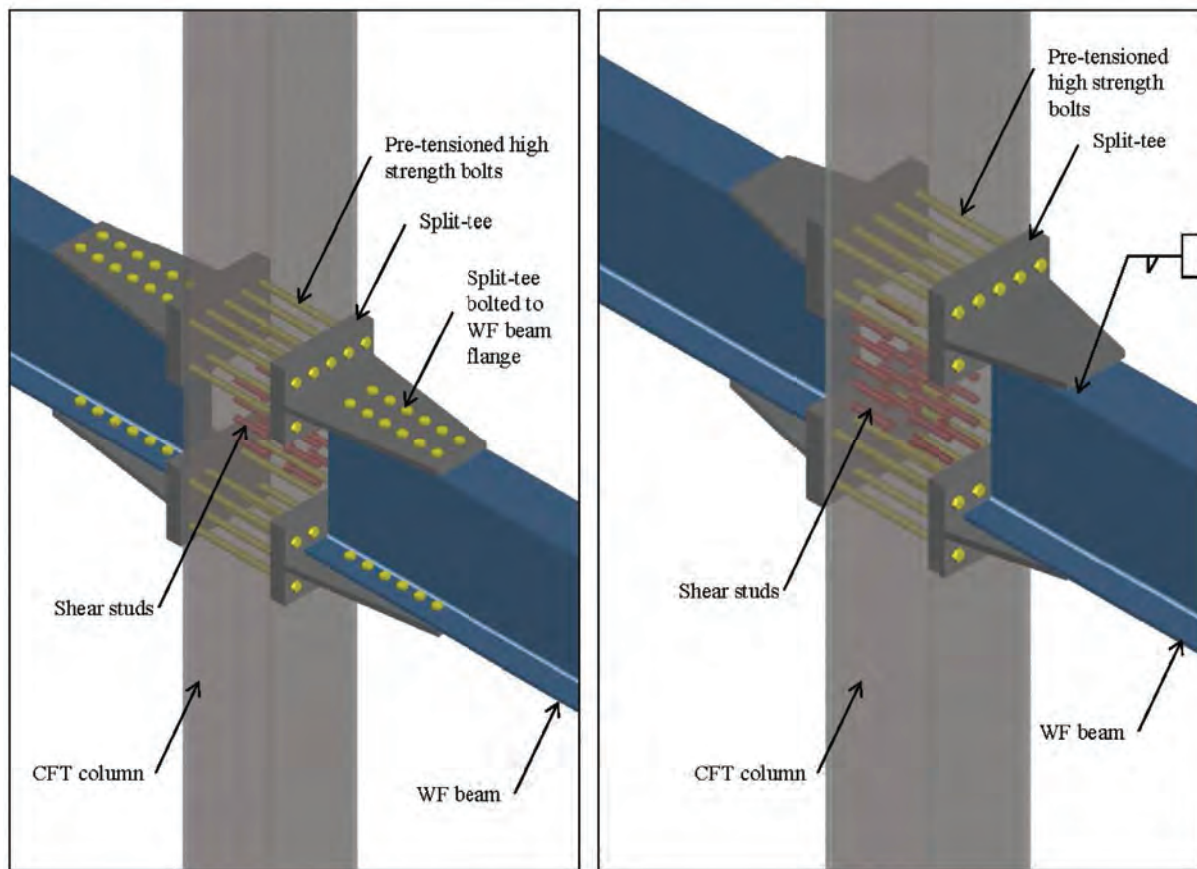


Fig. 1. Split-tee connection schematic of WF beam to CFT column (columns shown as transparent): (a) bolted split-tee connection; (b) welded split-tee connection.

EXPERIMENTAL DATA

The tests performed by Peng (2001) included a number of configurations for WF beam-to-rectangular CFT column connections. These also included the all-bolted and bolted-welded split-tee connections in Figure 1. The square CFT columns were 12-ft long, 16-in. \times 16-in. steel tube columns with 8-ksi concrete infill. The W24 \times 62 beams were 10 ft long. The specimens were designed as weak-beam, weak-panel zone or weak-connection specimens. Gravity loading (axial compression) was applied to the column first. It was followed by cyclic lateral loading in accordance with ATC-24 (Applied Technology Council [ATC], 1992) provisions; consisting of six elastic loading cycles, followed by inelastic displacement (or drift) cycles with increasing amplitude. Lateral bracing prevented out-of-plane movement of the connection region during the experiments.

Table 1 shows the connection types tested by Peng (2001) along with the ratio of the measured flexural resistance

at the connection, M_{max} , to the measured plastic flexural capacity of the connected beam calculated using measured material properties, $M_{p,meas}$. Specimens 1, 2, 3, 3R, 4, 5, 6 and 7 were weak-beam tests that formed plastic hinges in the beams outside of the connection regions. The maximum flexural resistance, M_{max} , at the connections for the weak-beam specimens ranged from 1.18 $M_{p,meas}$ for specimen 2 to 1.56 $M_{p,meas}$ for specimen 7.

Specimens 4 through 7 used split-tee moment connections. Specimen 4 had pinched hysteresis loops due to the slip between the split-tee and the WF beam top flange. Specimens 5, 6 and 7 used a welded washer detail to prevent this behavior. Specimen 5 was an all-bolted split-tee connection without a shear tab. It did not have bolt-hole elongation during cyclic testing and, therefore, no pinching of the hysteresis loops. Specimens 6 and 7, which were bolted-welded split-tee beam-to-column connections also showed the formation of plastic hinges in the beams. These plastic hinges included inelastic local buckling of the beam web and flanges with

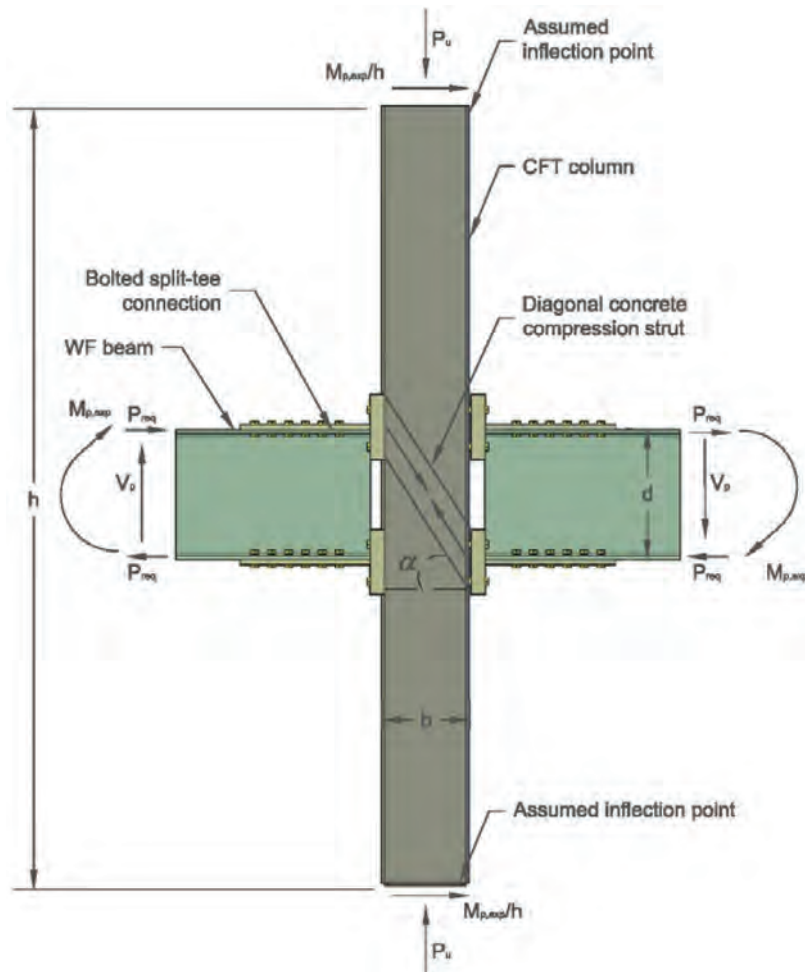


Fig. 2. Force transfer mechanism in split-tee connection along with panel zone in CFT.

Table 1. Test Matrix for Rectangular WF Beam-to-CFT Column Connection Experiments (Peng, 2001; Ricles et al., 2004)		
Specimen Number	Connection Detail	$\frac{M_{max}}{M_{p,meas}}$
1	Interior diaphragms (four-sided weld)	1.25
1R	Retrofitted interior diaphragms (four-sided weld), weak beam	1.08
1R2	Interior diaphragms with tapered plates (four-sided weld), weak-panel zone	1.03
2	Interior diaphragms (three-sided weld), weak beam	1.18
2R	Interior diaphragms with tapered plates (three-sided weld), weak-panel zone	0.89
3	Extended tee, weak beam	1.21
3R	Extended tee with tapered plates, weak beam	1.23
4	Bolted split-tee connection with shear tab, weak beam	1.34
5	Bolted split-tee connection without shear tab, weak beam	1.29
6	Welded split-tee connection without shear tab, weak beam	1.44
7	Welded split-tee connection with shear tab, weak beam	1.56

increasing inelastic deformations (story drifts). Flange local buckling eventually extended into the split-tee stem, with increasing story drifts. At story-drift angle of 0.05 rad, two cracks were observed in the specimen: (1) a crack in the beam top flange at approximately 1.5 in. from the edge of the split-tee stem and (2) a crack in the beam bottom flange approximately 2 in. from the edge of the split-tee stem. Specimens 4 through 7 all showed local yielding at the base of the split-tee stem during inelastic deformation cycles.

There was limited panel-zone shear yielding observed in the split-tee connection specimens (specimens 4 through 7). Because the through bolts connecting the split-tee to the CFT column were pretensioned, limited prying action of the split-tees was observed during the test.

Figure 3 shows the story-drift angles corresponding to the maximum load as well as 0.8 M_p (post-peak) for all the tested specimens. As shown, except for specimens 1, 1R and 2R, all other specimens met the AISC *Seismic Provisions* requirements for composite intermediate moment frames (C-IMFs) by having story-drift angles exceeding 0.02 rad at 0.8 M_p . Additionally, specimens 4, 5, 6 and 7 met the AISC *Seismic Provisions* requirements for C-SMFs by having story-drift angles exceeding 0.04 rad at 0.8 M_p . The full-scale tests demonstrated that split-tee moment connections could develop the expected plastic moment capacity, $M_{p,exp}$, of the beams, and accommodate story-drift angles exceeding 0.04 rad while maintaining (post-peak) flexural resistance at 0.8 M_p .

SPLIT-TEE CONNECTION DESIGN EXAMPLE

Section G3 of the AISC *Seismic Provisions* states that the basis of design for C-SMFs is that the frame will provide

significant inelastic deformation capacity through flexural yielding of the C-SMF beams and limited yielding of the column panel zone. Flexural yielding of the column bases is permitted. The split-tee design example presented in this section assumes that plastic hinges form in the WF beams outside of the protected connection zone. The failure modes of split-tee connections are listed here in order, from most ductile to least ductile:

1. Plastic hinge formation in beam.
2. Stem yielding of split-tee.
3. Flange yielding of split-tee due to prying action.
4. Panel-zone failure of column.
5. Bolt fracture in split-tee due to prying action of split-tee flange.

The following example presents the design procedure for split-tee connections bolted to the CFT columns and welded to WF beams. The split-tee connection is designed and detailed to resist the expected shear force due to the expected plastic moment capacity of the beam and the gravity loads. The connection is also designed and detailed so that the governing failure modes occur in the just-listed order 1 through 5 from most ductile (desirable) to least ductile. Figures 4 through 12 provide a step-by-step approach for designing this connection. In this example, the beams are W24×76 ASTM A992 wide-flanged sections that are 30 ft in length ($F_y = 50$ ksi, $F_u = 65$ ksi, $R_y = 1.1$), and the CFT column is HSS16×16×0.75 made from ASTM A500 Grade B steel ($F_y = 46$ ksi, $F_u = 65$ ksi) and filled with normal-weight, 7-ksi concrete ($f'_c = 7$ ksi). The gravity loads considered on the beam are 0.84 kip/ft distributed dead load

Width of column, B	16 in.
Depth of column, h	16 in.
Thickness of web of column, t_w	0.75 in.
Depth of beam, d	23.9 in.
Width of beam flange, b_f	8.99 in.
Thickness of beam web, t_w	0.44 in.
Thickness of beam flange, t_f	0.68 in.
Beam plastic section modulus, Z_x	200 in. ³

and 0.60 kip/ft distributed live load. The dimensions of the beam and column sections taken from the 14th edition AISC *Steel Construction Manual* are shown in Table 2.

Figure 4 shows the final dimensions and details for the split-tee connection. Figure 5 shows the general procedure for design and detailing split-tee connections. This procedure addresses the primary failure modes (1 through 5 mentioned earlier) and references Figures 5 through 12, which specifically address each of these failure modes and provide procedures for detailing split-tee connections. The following steps provide an overview of split-tee connection design and a description of each of the Figures 6 through 12.

- Step 1: Calculate the flexural and shear demands for the connection at the face of the column. Figure 6 provides the procedure for calculating these demands using the expected plastic flexural capacity, $M_{p,exp}$, of the beams and the gravity loads on the structure. Calculate the flange forces in the split-tee connection. Figure 6 shows how to calculate the flange forces from the flexural demand.
- Step 2: Determine the number of pretensioned through bolts required to resist the flange forces in the connection. The bolts are sized to resist the shear demand calculated in step 1 and the flange forces calculated in step 1.
- Step 3: Establish the layout of pretensioned through bolts in the split-tee flanges to satisfy force-equilibrium equations. The force-equilibrium equations are based upon the geometry of the split-tee as shown in Figure 7.
- Step 4: Design the thickness of the split-tee stem. Consider failure modes of stem fracture and stem yielding.
- Step 5: Determine the minimum flange width based on the bolt layout determined in step 3.
- Step 6: Design the thickness of the split-tee flange so

that stem yielding of the split-tee occurs prior to bolt fracture due to prying forces. The maximum thickness of the split-tee flange is determined to prevent bolt fracture due to prying forces prior to yielding of the split-tee flanges. The minimum thickness of the split-tee flange is determined so that split-tee stem yielding occurs prior to bolt fracture. (See Figure 8.)

- Step 7: Detail the final dimensions of the connection based upon the minimum and maximum split-tee flange and stem thicknesses calculated in steps 4, 5 and 6.
- Step 8: Calculate the actual flange forces in the connection based upon the final geometry of the connection detailed in step 7.
- Step 9: Calculate prying forces in the flanges of the split-tee using the final dimensions of the connection. Yielding of the split-tee flanges due to prying should occur prior to bolt fracture as a potential failure mechanism. Figure 9 shows the procedure for checking the final dimensions of the split-tee connection for this.
- Step 10: Figure 10 shows the steps for checking the detailed geometry for stem fracture, stem yield, balanced failure (split-tee stem yielding before flange yielding) and shear.
- Step 11: Figure 11 shows the procedure for sizing the weld between the split-tees and the WF beam flanges based on the thicknesses of the connecting material and the flange forces calculated in step 8.
- Step 12: Figure 12 shows the calculations for the panel-zone shear strength of the CFT column. The shear strength of the panel zone should be greater than the flange forces calculated in step 8. This is consistent with the initial assumption that plastic hinge formation occurs in the WF beams of the C-SMF.

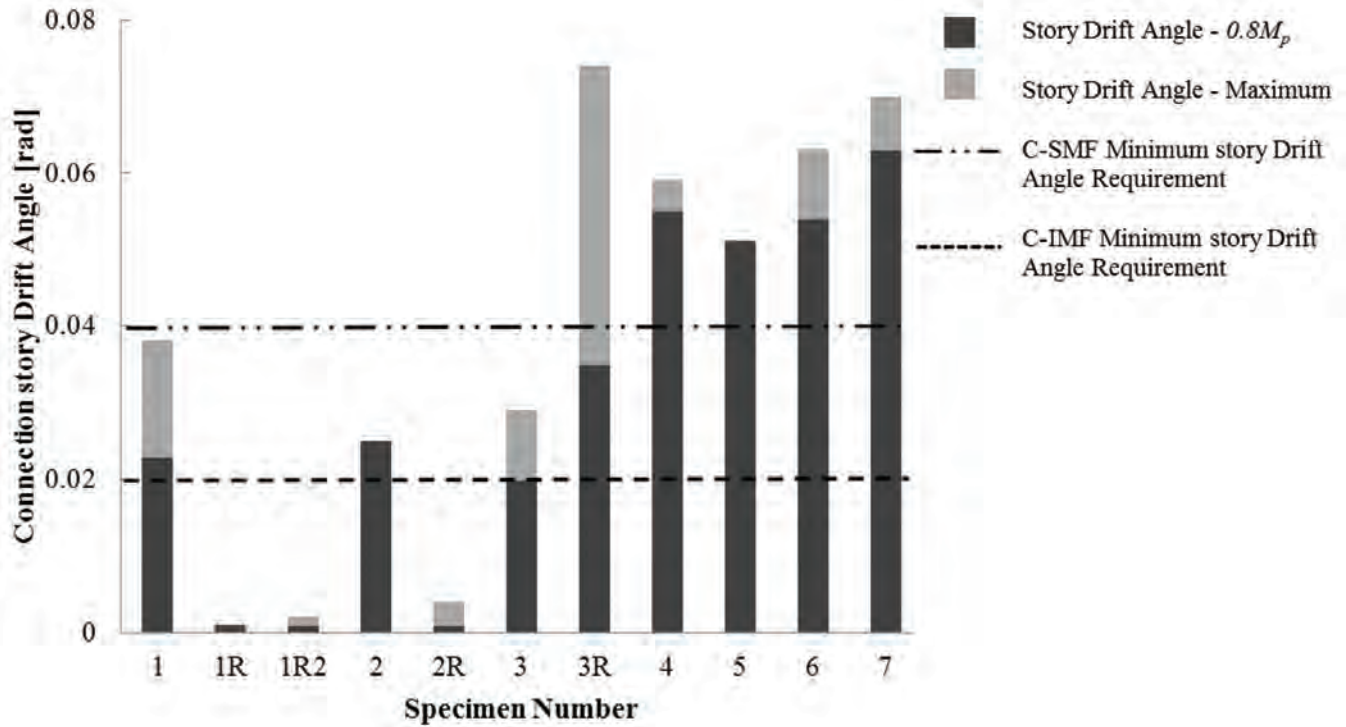


Fig. 3. Summary of story-drift angle for connections tested (Peng, 2001).

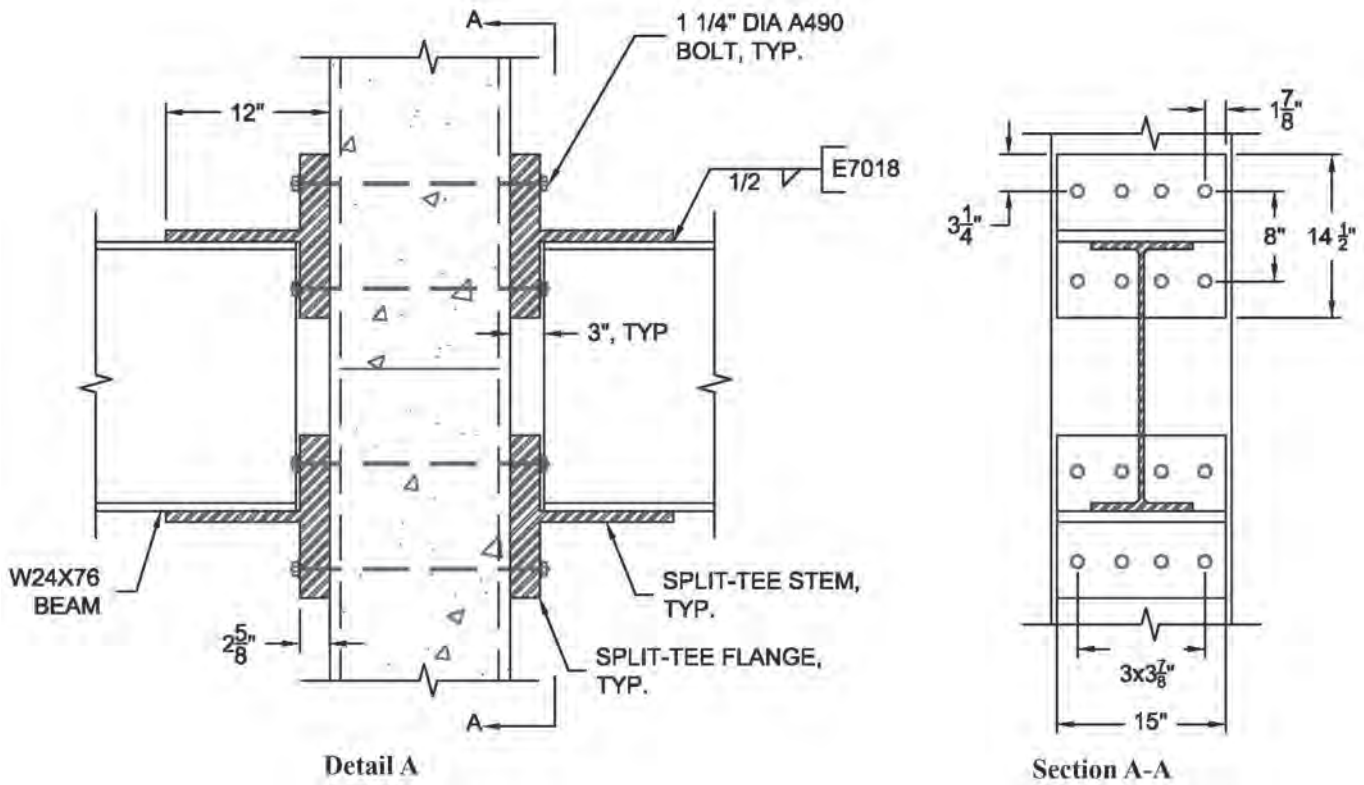


Fig. 4. Split-tee connection detail.

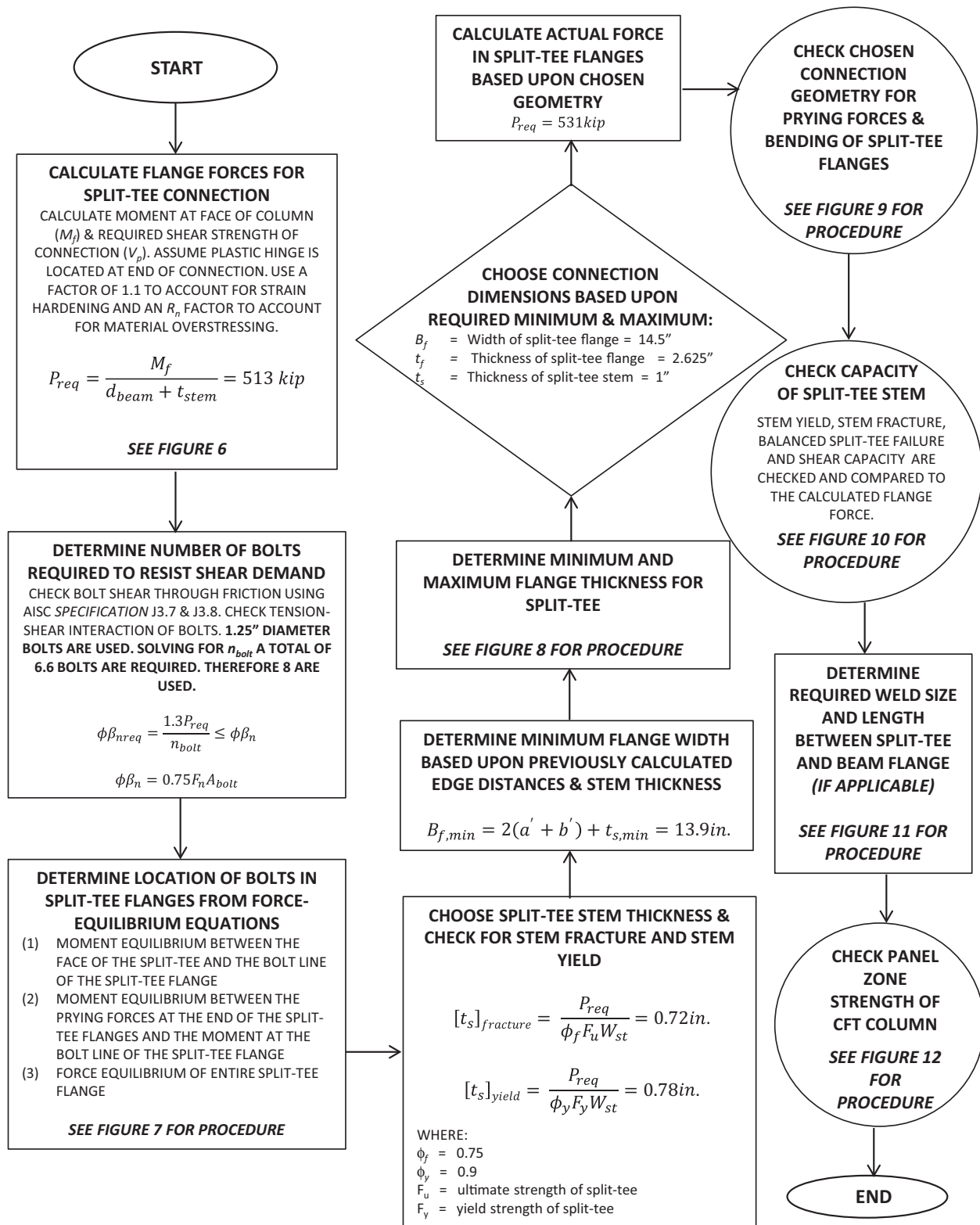


Fig. 5. Main flow chart for split-tee connection design.

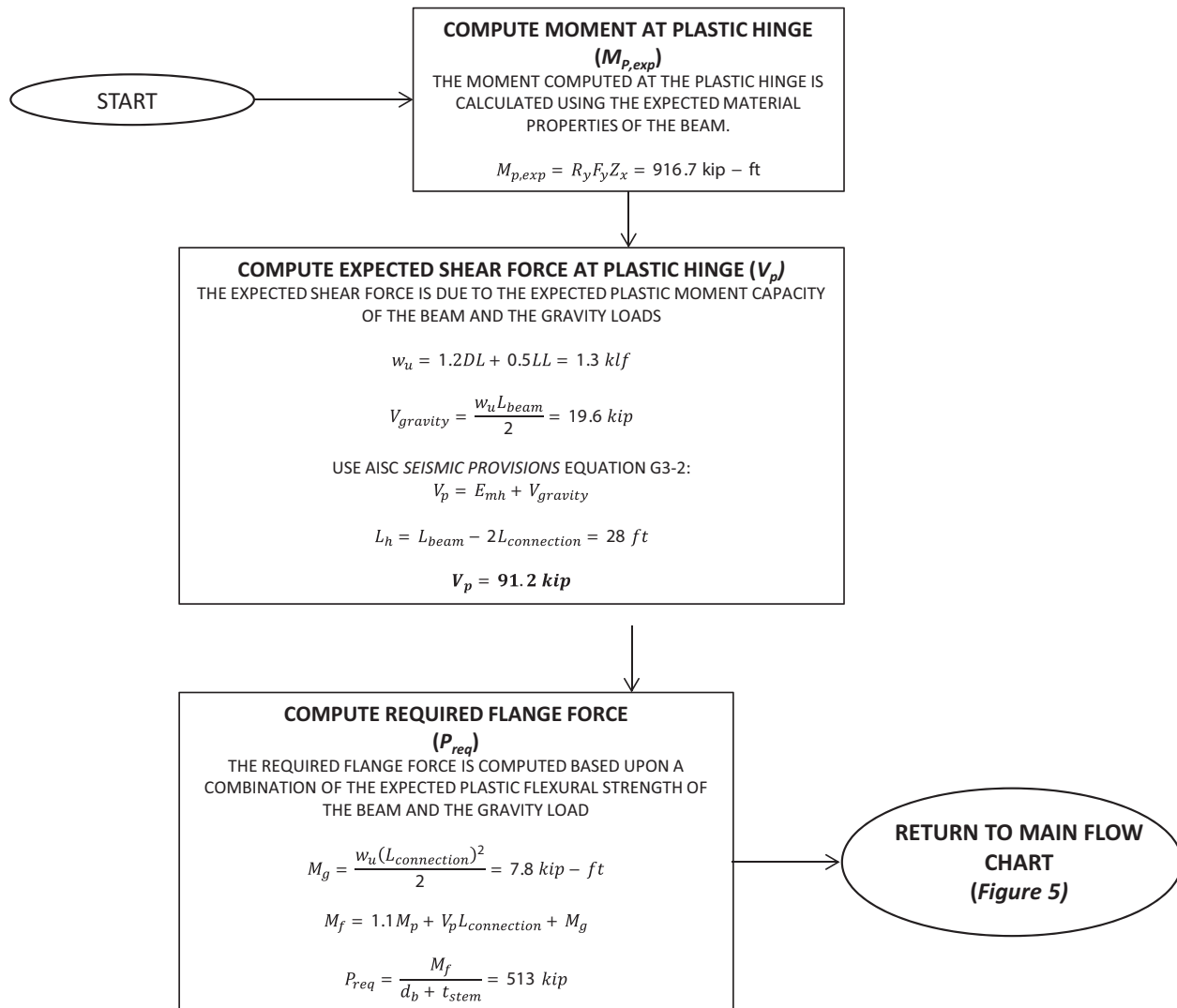
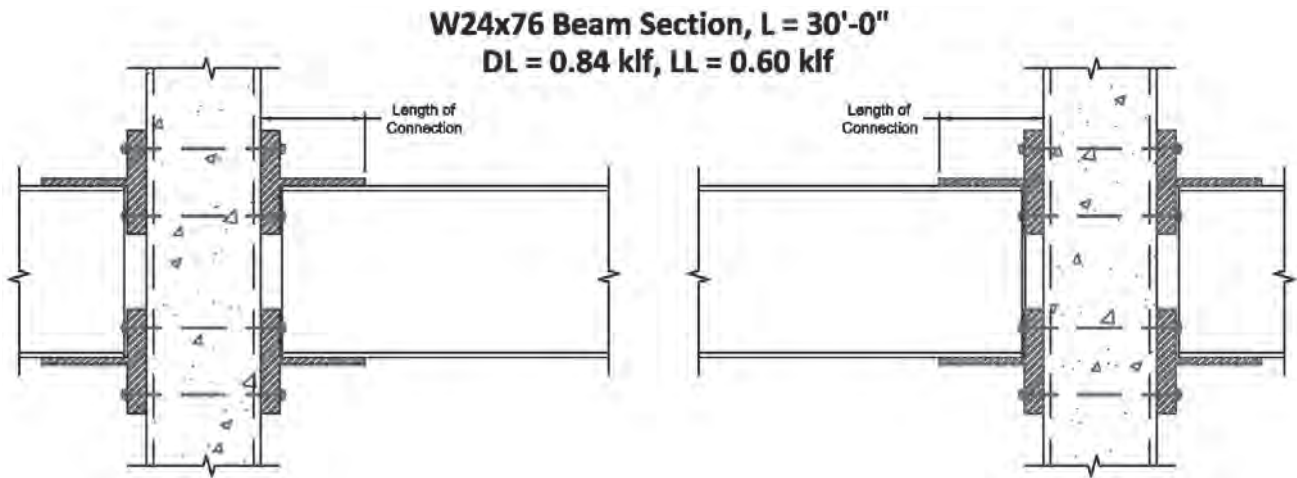
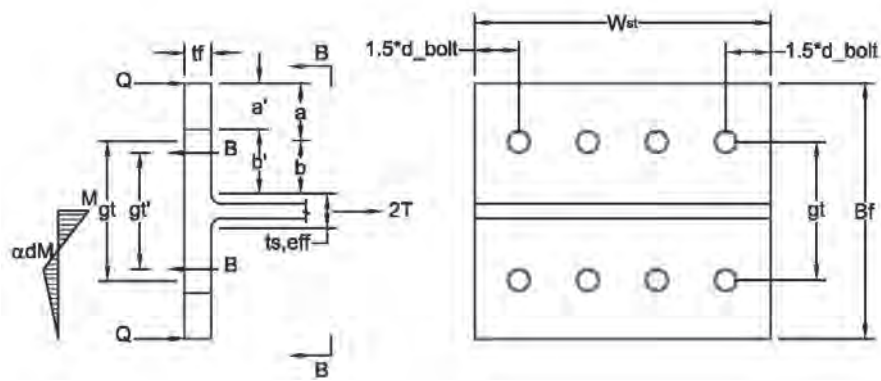


Fig. 6. Calculate moment at the face of the column and required shear strength of the connection.



(a) SPLIT-TEE GEOMETRY & FORCES

SECTION B-B
(b) SPLIT-TEE GEOMETRY

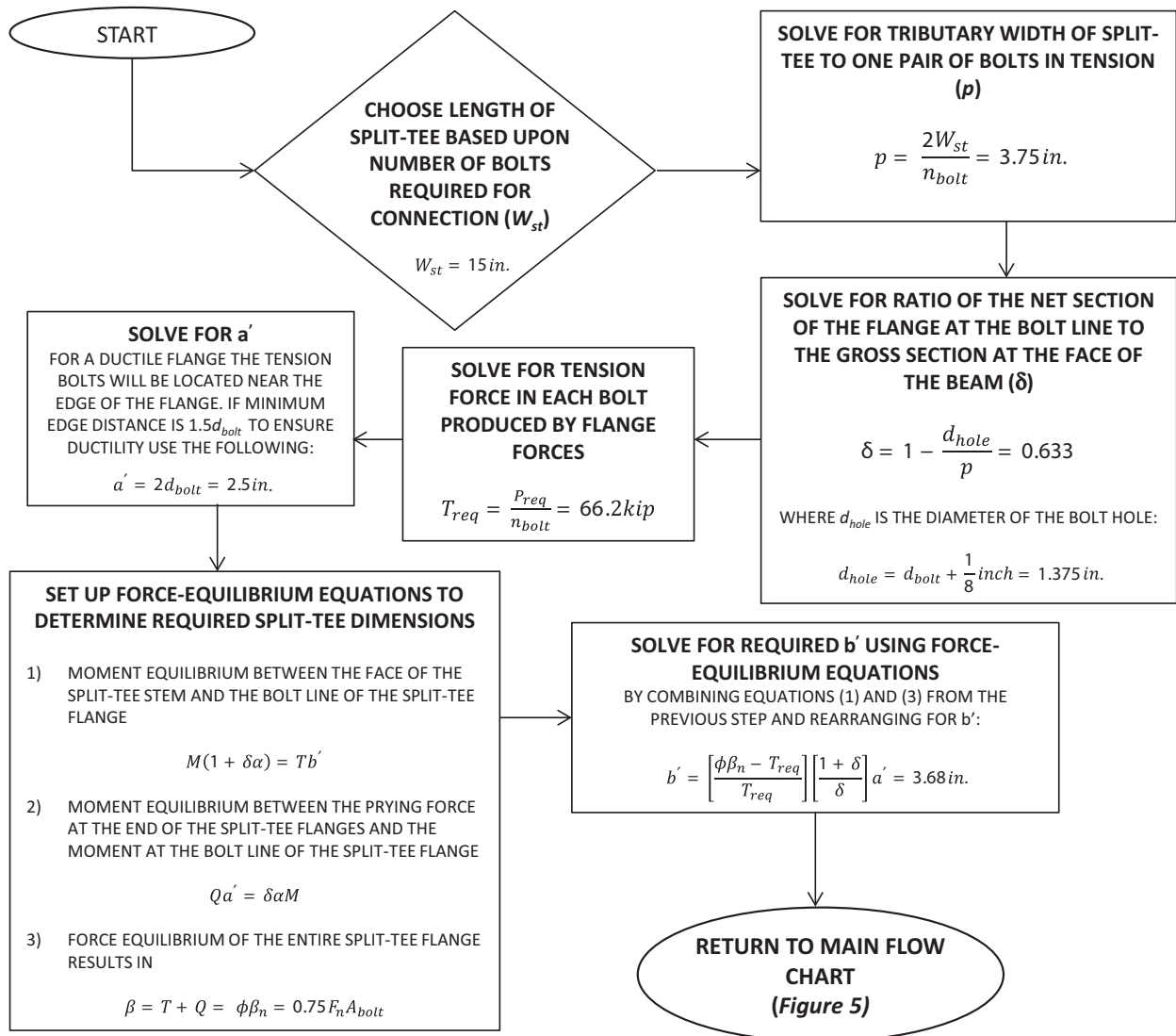


Fig. 7. Force equilibrium equations for location of bolts.

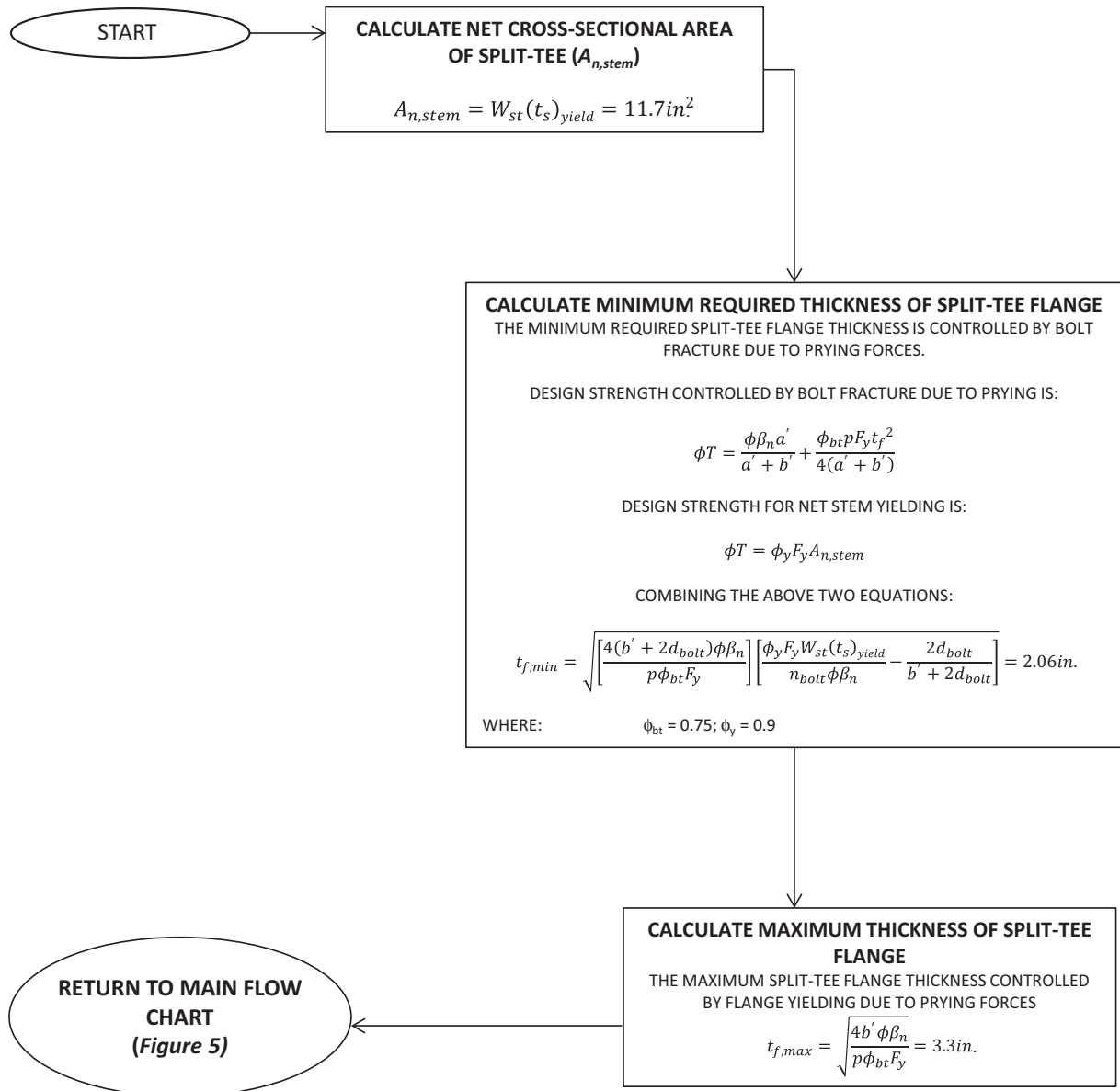
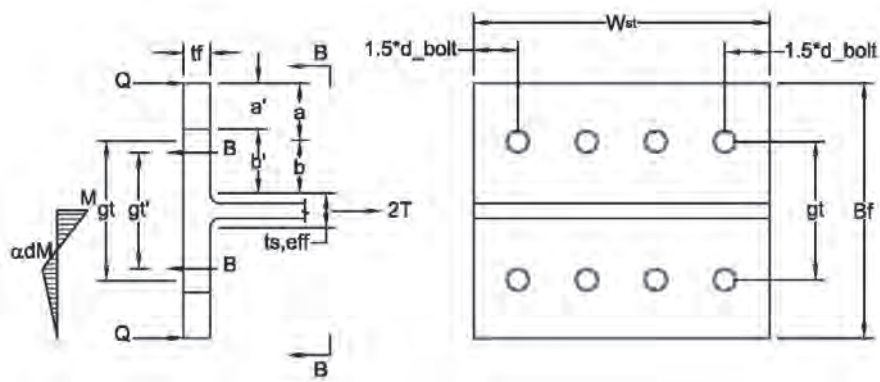


Fig. 8. Check minimum and maximum flange thickness for split-tee.



(a) SPLIT-TEE GEOMETRY & FORCES

SECTION B-B
(b) SPLIT-TEE GEOMETRY

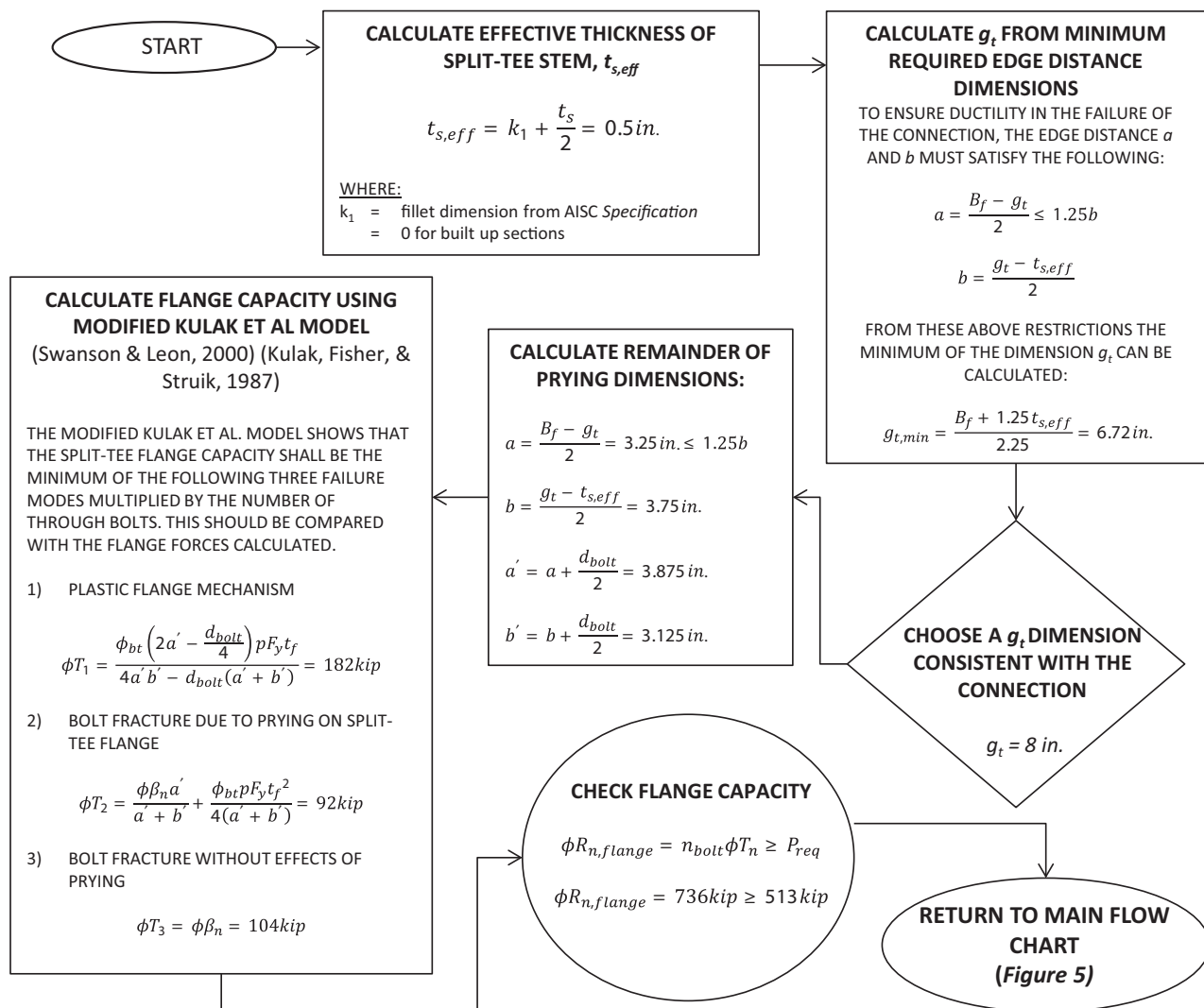


Fig. 9. Check prying forces and flange bending on split-tee.

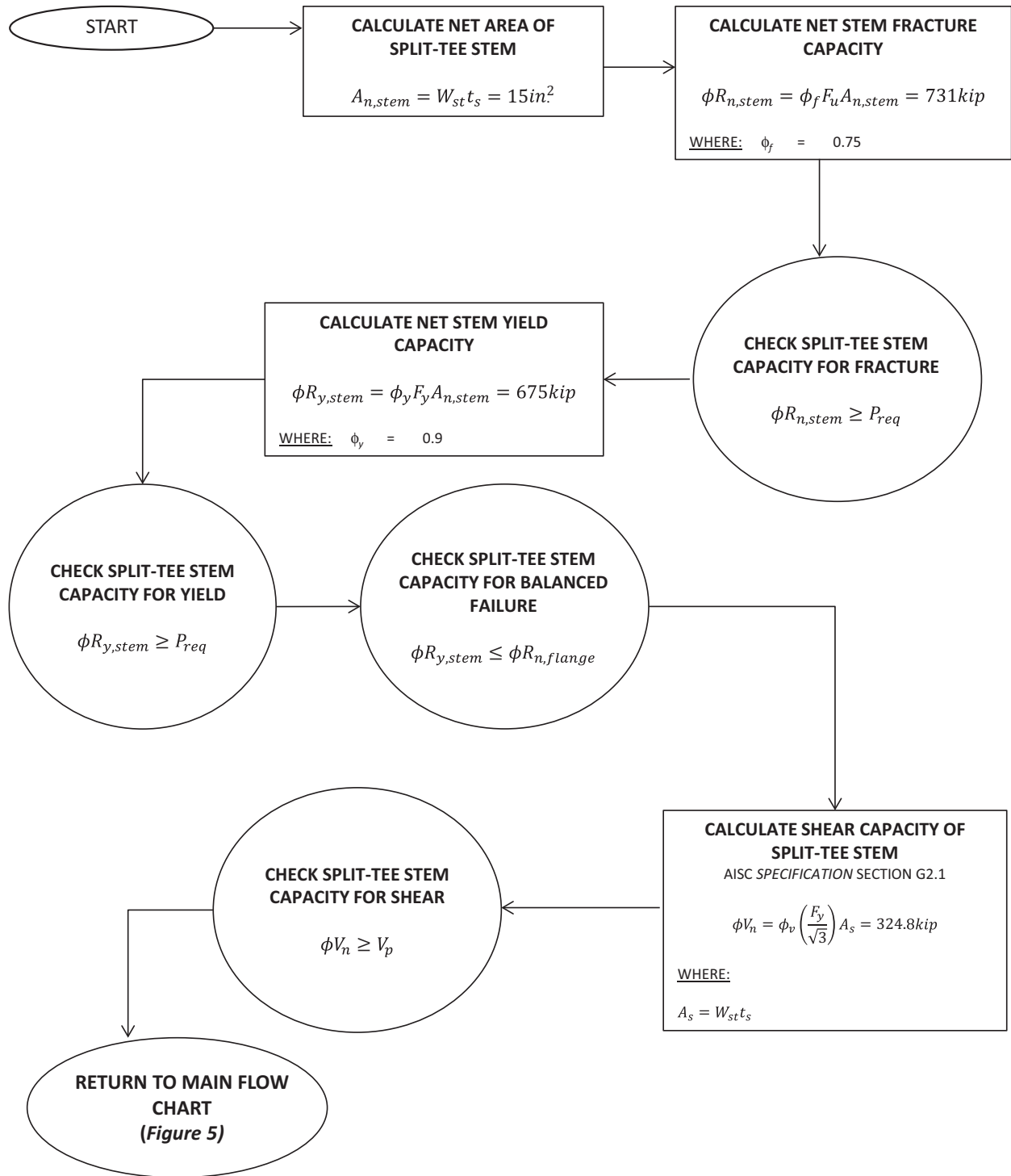


Fig. 10. Split-tee stem capacity check.

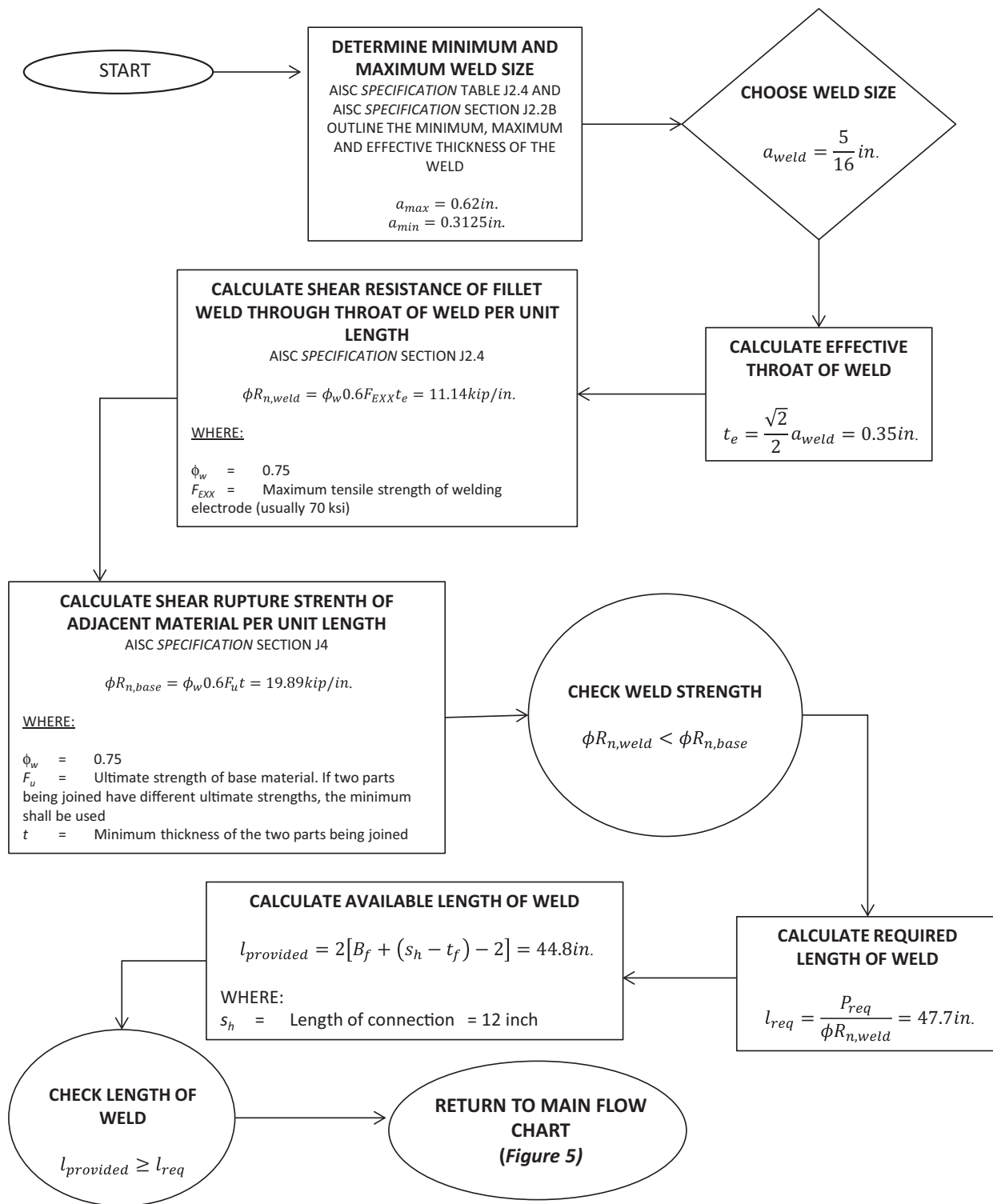


Fig. 11. Fillet weld at split-tee stem and beam flange.

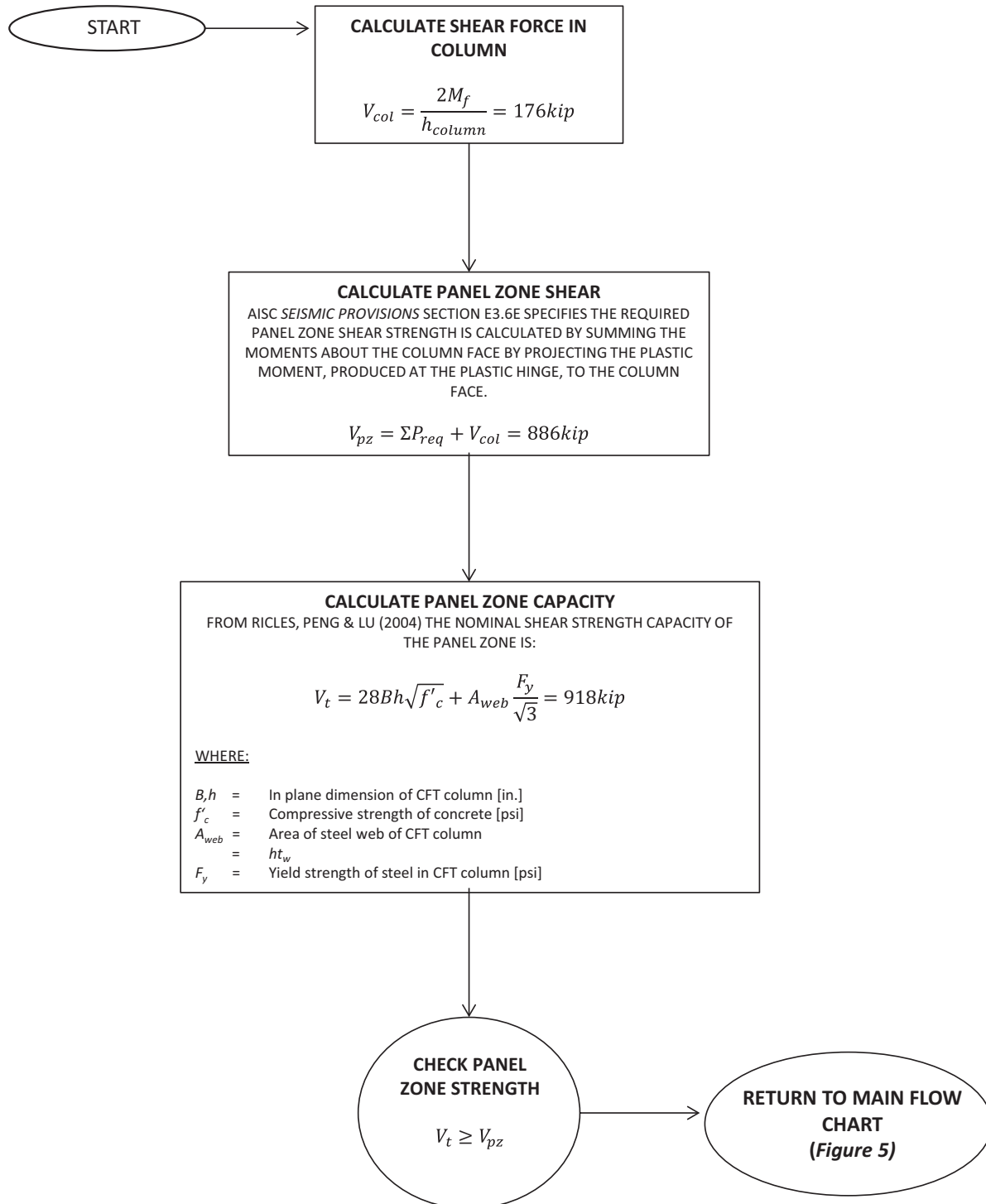


Fig. 12. Check panel zone of CFT column.

SUMMARY AND CONCLUSIONS

The experimental program conducted by Peng (2001) showed that split-tee connections satisfy the requirements of the AISC *Seismic Provisions* (AISC, 2010a) for beam-to-column moment connections in C-SMFs. The all-bolted split-tee connection had pinching in the cyclic (hysteresis) response due to elongation of the bolt holes and slipping between the stems of the split-tee and the WF beam flanges. The bolted-welded split-tee connection resolved this (pinching) issue by welding the split-tee stem to the WF beam flanges.

The AISC *Prequalified Connections* (AISC, 2010b) does not include examples of beam-to-column connections for C-SMF construction. The engineer is required to create a "Prequalified Record" for the designed beam-to-column connection. This paper along with the test results from Peng (2001) provides many of the necessary sections for the "Prequalified Record" outlined in Section K1.6 of the AISC *Seismic Provisions*, including the following:

- A general description of the prequalified connection.
- A description of expected behavior of the connection in the elastic and inelastic ranges.
- A definition of connection region that comprises the protected zone.
- A detailed description of the design procedure for the connection.
- A list of references of test reports, research reports and other publications that provide basis for prequalification.

This paper presented a comprehensive design procedure and associated design example for bolted-welded split-tee connections in C-SMFs. The design procedure accounts for the potential failure modes of the connection and organizes them in hierarchal order from most ductile (desirable) to least ductile, namely: (1) plastic hinge formation in beam, (2) stem yielding of the split-tee, (3) flange yielding of split-tee due to prying action, (4) panel-zone failure of column and (5) bolt fracture due to prying action of split-tee. Both the design procedure and the design example establish plastic hinge formation in the WF beams outside of the connection region as the controlling limit state for the split-tee moment connection. The comprehensive design procedure and example are illustrated using flowcharts in Figures 5 through 12.

SYMBOLS

Beam and Column Dimensional Notation

B	Width of column (in.)
F_u	Ultimate stress of steel (ksi)
F_y	Yield stress of steel (ksi)
R_y	Material correction factor
b_f	Width of beam web (in.)
d	Depth of beam (in.)
f'_c	Compressive stress of concrete (ksi)
h	Depth of column (in.)
t_f	Thickness of beam flange (in.)
t_w	Thickness of column or beam web (in.)

Split-tee Notation

B_f	Width of split-tee flange (in.)
$L_{connection}$	Length of the connection (in.)
W_{st}	Depth of split-tee (in.)
Z_x	Plastic section modulus (in. ³)
t_f	Thickness of split-tee flanges (in.)
t_s	Thickness of split-tee stem (in.)
t_{stem}	Assumed thickness of split-tee stem (in.)

Capacity Notation

$[t_s]_{fracture}$	Minimum required stem thickness for fracture limit state (in.)
$[t_s]_{yield}$	Minimum required stem thickness for yield limit state (in.)
A_{bolt}	Area of bolt
$A_{n,stem}$	Net area of stem (in. ²)
$B_{f,min}$	Minimum flange width (in.)
F_n	Nominal stress of bolt (ksi)
M_f	Moment at face of column (k-ft)
M_p	Plastic flexural strength using nominal material properties (k-ft)
$M_{p,exp}$	Plastic flexural strength using expected material properties (k-ft)
$M_{p,meas}$	Plastic flexural strength using measured material properties (k-ft)

P_{req}	Required flange forces for double split-tee connection design (kip)
V_{col}	Shear force in column (kip)
V_{pz}	Shear force in panel zone (kip)
V_t	Column panel-zone capacity (kip)
α_{max}	Maximum required weld size (in.)
α_{min}	Minimum required weld size (in.)
α_{weld}	Actual weld size (in.)
$l_{provided}$	Provided length of weld (in.)
l_{req}	Required length of weld (in.)
n_{bolt}	Number of bolts
t_e	Effective throat of weld (in.)
$\phi R_{n,base}$	Shear rupture strength of adjacent material per unit length (kip/in.)
$\phi R_{n,flange}$	Flange capacity of split-tee (kip)
$\phi R_{n,stem}$	Net stem fracture capacity (kip)
$\phi R_{n,weld}$	Fillet weld shear resistance through throat of weld per unit length (kip/in.)
$\phi R_{y,stem}$	Net stem yield capacity (kip)
ϕV_n	Shear capacity of split-tee stem (kip)
$\phi \beta_n$	Capacity of bolt (kip)
$\phi \beta_{nreq}$	Required capacity of bolt (kip)

REFERENCES

- American Institute of Steel Construction, Inc. (2010a), *Seismic Provisions for Structural Steel Buildings*, ANSI/AISC 341-10, Chicago, IL.
- American Institute of Steel Construction, Inc. (2010b), *Prequalified Connections for Special and Intermediate Steel Moment Frames for Seismic Applications*, ANSI/AISC 358-10, Chicago, IL.
- American Institute of Steel Construction, Inc. (2010c), *Specification for Structural Steel Buildings*, ANSI/AISC 360-10, Chicago, IL.
- American Institute of Steel Construction, Inc. (2011), *Steel Construction Manual*, 14th Ed., Chicago, IL.
- Applied Technology Council (1992). "Guidelines for Seismic Testing of Components of Steel Structures," Redwood City, CA.
- Kanno, R. and Deierlein, G.G. (1997), "Seismic Behavior of Composite (RCS) Beam-Column Joint Subassemblies," *Composite Construction III*, ASCE, Reston, VA.
- Kulak G., Fisher, J. and Struik, J. (1987), *Guide to Design Criteria for Bolted and Riveted Joints*, Indianapolis: John Wiley & Sons, Inc.
- Lai, Z., Varma, A.H. and Zhang, K. (2014), "Noncompact or Slender Rectangular CFT Members: Experimental Database, Analysis and Design," *Journal of Constructional Steel Research*, Vol. 101, pp. 455–468.
- Peng, S.W. (2001), "Seismic Resistant Connection for Concrete-Filled Tube Column-to-WF Beam Moment Resisting Frames," Ph.D. Dissertation. Bethlehem, PA: Lehigh University.
- Ricles, J.M., Peng, S.W. and Lu, L.W. (2004), "Seismic Behavior of Composite Concrete Filled Steel Tube Column-Wide Flange Beam Moment Connections," *Journal of Structural Engineering*, Vol. 130, pp. 223–232.
- Schneider, S.P. and Alostaz, Y.M. (1998), "Experimental Behavior of Connections to Concrete-filled Steel Tubes," *Journal of Constructional Steel Research*, Vol. 45, No. 3, pp. 321–352.
- Swanson J.A. and Leon, R.L. (2000), "Bolted Steel Connections: Tests on T-Stub Components," *Journal of Structural Engineering*, Vol. 126, pp. 50–56.
- Varma, A.H., Ricles, J.M., Sause, R. and Lu, L.W. (2002), "Seismic Behavior and Modeling of High Strength Composite Filled Steel Tube Beam-Columns," *Journal of Constructional Steel Research*, Vol. 58, No. 5–8, pp. 725–758.

Structural Innovation: Combining Classic Theories with New Technologies

WILLIAM F. BAKER, LAUREN L. BEGHINI, ARKADIUSZ MAZUREK, JUAN CARRION and ALESSANDRO BEGHINI

Baker received AISC's T.R. Higgins Lectureship Award in 2013. Learn more about this prestigious award at www.aisc.org/higgins.

ABSTRACT

In the early stages of the design process, an engineer sets the geometry of the structure. The decisions made about the layout of the structure will determine the overall efficiency that can be achieved and the magnitude of the forces that must be accommodated. For example, the deflection of a truss can actually be decreased by removing material if a geometry is created that has a shorter total load path. This paper presents concepts and methodologies for creating and understanding efficient geometries. It starts with a review of the 19th- and 20th-century load path theories of Rankine, Maxwell, Cremona and Michell. It then combines their insights with current topology optimization and shape-finding tools as a means of exploring how engineers can create structural geometries that improve the behavior and reduce the tonnage of their designs. Several examples of classical theoretical solutions are explored along with their application to new designs.

Keywords: structural geometry, structural efficiency, structural analysis.

INTRODUCTION

The success of any project depends on starting with a good concept. For the design of structural steel trusses and other structures, the geometrical arrangement of the members is often the most important consideration in producing an efficient and well-behaved design. Although efficiency has always been a chief design consideration, its importance has increased lately as designers seek to minimize the carbon footprint in the construction of new structures. Where can the designer seek guidance in creating layouts that achieve the goals of efficiency and good behavior? A good place to begin is at the start of modern structural engineering.

The mid-19th century was a key period in the advancement of the understanding of structural behavior. The theory of elasticity had already been highly advanced through the development of elastic "aether" theories, and many mathematicians, scientists and natural philosophers were

extending their studies into structural mechanics, as well as optics, electricity and magnetism. Their interest in structures was undoubtedly further influenced by the advent of the railroad.

The emergence of railroads led to technological challenges and advancements. The railroads needed bridges and, as a response, the first metal truss bridge was built in the United States in 1840 and in the United Kingdom in 1845 (Timoshenko, 1953). The great thinkers of the time began focusing their thoughts upon the practical issues of trusses and bridges and, in doing so, pushed the limits of structural engineering. One such example is the British Astronomer Royal, George Biddell Airy, who not only studied the stars, but also developed his famous Airy stress function in response to Stephenson's Britannia Bridge (Airy, 1863).

This paper reviews some important works by Rankine, Maxwell, Cremona and Michell that still have great relevance to modern design. Today's structural engineer can combine the ideas of these great innovators with modern topology optimization tools to develop structural concepts for steel trusses and other structures. By combining these concepts with practical considerations of constructability and cost, the structural engineer can develop responsible designs that can minimize the carbon footprint in the construction of new structures and help reduce the consumption of our natural resources.

Please note the theories and findings included in this paper are based on equilibrium and compatibility and, when calculating volume, strength or deflection, constitutive relationships assuming linearly elastic material. The analysis and exploration of the effects of geometric and material nonlinearities on optimal topology layouts is under investigation by a number of researchers.

William F. Baker, P.E., S.E., Partner, Skidmore, Owings & Merrill LLP, Chicago, IL (corresponding). Email: william.baker@som.com

Lauren L. Beghini, Ph.D., Structural Engineer, Skidmore, Owings & Merrill LLP, Chicago, IL. Email: lauren.beghini@gmail.com

Arkadiusz Mazurek, Ph.D., P.E., S.E., Associate, Skidmore, Owings & Merrill LLP, Chicago, IL. Email: arkadiusz.mazurek@som.com

Juan Carrion, Ph.D., P.E., Structural Consultant, Skidmore, Owings & Merrill LLP, Chicago, IL. Email: juan.carrion@som.com

Alessandro Beghini, Ph.D., P.E., S.E., Associate, Skidmore, Owings & Merrill LLP, San Francisco, CA. Email: alessandro.beghini@som.com

Paper No. 2014-14

MAXWELL'S THEOREM ON LOAD PATHS

When famously asked if he had stood on the shoulders of Newton, Albert Einstein replied, "That statement is not quite right. I stood on Maxwell's shoulders" (Forfar, 2012). James Clerk Maxwell was one of the greatest thinkers of the 19th century and, although best known for his work in electromagnetic theory, his influence extends to various other scientific subjects, including significant work in structural engineering.

In his 1864 paper, "On Reciprocal Figures and Diagrams of Forces," Maxwell [who begins his paper with a reference to Rankine's (1864) work on the equilibrium of polyhedral trusses] developed a theorem that essentially states that the sum of a structure's tension load paths minus the sum of the compression load paths is equal to a value related to the applied external forces (including reactions). In this paper, the term *load path* for a structure or group of members refers to the sum of the axial force in each member times its length. Expressed as an equation, Maxwell's theorem can be written as follows (Cox, 1965):

$$\sum F_T L_T - \sum F_C L_C = \sum \bar{P}_i \cdot \bar{r}_i \quad (1)$$

The value on the right side is the dot product of all the external forces, \bar{P}_i , with position vectors from an arbitrary origin, \bar{r}_i . This dot product ($\sum \bar{P}_i \cdot \bar{r}_i = |\bar{P}_i| |\bar{r}_i| \cos \theta$, where θ is the angle between vectors \bar{P}_i and \bar{r}_i) can be viewed as a representation of the negative of the work it takes for all the external forces to cancel all the reactions. Its proof is straightforward: If there is a truss with a series of applied external loads that are in equilibrium with a set of internal forces (see Figure 1) and, from an arbitrary point, if the space is dilated so that all the nodes become twice as far from the origin as they were originally, all the tension forces will do positive work equal to the tensile force in each member times the member length. The compression members will also double in length but will do negative work. From conservation of energy, the total internal work will be equal to the work done by the external forces, which is equal to the dot product on the right side.

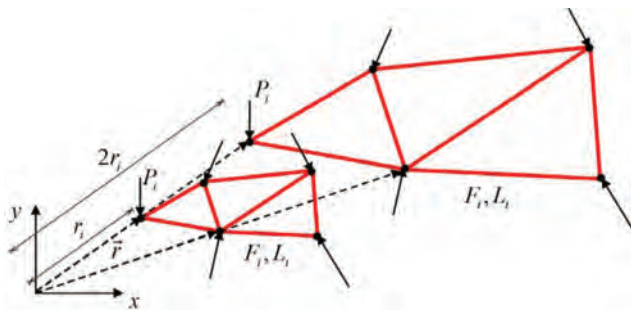


Fig. 1. Geometrical proof of Maxwell's theorem.

While this theorem has generally been lost to the engineering profession, it represents a very powerful idea that has great potential in the design of trusses. It tells us that the longer the total tension load path, the longer the compression load path must be for a set of external loads of given magnitude, direction and position. Stated another way, if a tension (or compression) load path is "too long," the truss will be penalized twice—once in tension and once in compression. Thus, if we can find a configuration that minimizes the tension load path, the compression load path will automatically be minimized and vice versa.

A further observation is that if a structure only has tension members or only has compression members, it is already a structure of minimal load path, assuming that the points of applied loads and reactions do not change as the geometry of the structure changes.

Figure 2 shows an illustration of Maxwell's theorem using the loads and supports of a cantilever with a 3:1 span. If the origin is placed at the lower left point of the cantilever, the dot product can be easily calculated and is equal to PB . Thus, according to Maxwell's theorem, the difference between the tension load path and the compression load path is PB .

It can also be shown that the constant PB represents the negative of the work needed for the applied loads and reactions to cancel each other. For example, by moving the two horizontal forces together to cancel one another, zero work is done because the movement is perpendicular to the direction of the forces. Furthermore, if the vertical force at the lower right of the cantilever were to be moved and placed directly below the upper vertical load, zero work is still done but, as this load is moved to the point in which the vertical loads are canceled, negative work equal to Maxwell's constant PB is done.

LOAD PATHS OF DIFFERENT TRUSS GEOMETRIES

The efficiency of the cantilever constructed to carry the loads shown in Figure 2 can be examined by considering a series of different truss geometries. For example, the first considered geometry might be the moment diagram, which, although it has the shortest path, is not the shortest



Fig. 2. Illustration of Maxwell's theorem using a 3:1 cantilever.

load path structure (Figure 3). Here, the force in the tension member times its length gives the total tensile load path $\sum F_T L_T = 10PB$, while the force in the compression member times its length results in a total compressive load path of $\sum F_C L_C = 9PB$, resulting in a difference of $\sum F_T L_T - \sum F_C L_C = PB$, as predicted by Maxwell's theorem. The total load path is $\sum F_T L_T + \sum F_C L_C = 19PB$. But how much would such a truss deflect? Using the Principle of Virtual Work, the deflection can be expressed as follows:

$$\Delta = \sum \frac{nFL}{EA} \quad (2)$$

and, if this is a fully stressed structure with equal stresses in tension and compression, the truss will deflect by $19\sigma B/E$.

Another classic solution to the 3:1 cantilever is the Pratt truss (Figure 4). Here, the summation of the tension member forces times their corresponding lengths is $\sum F_T L_T = 9PB$, and the summation of the compression member forces times their corresponding lengths is $\sum F_C L_C = 8PB$. The difference is once again Maxwell's constant, PB , but the total load path has decreased to $17PB$, while the deflection has decreased to $17\sigma B/E$. Although the Pratt truss has a higher total length of members, it has a shorter load path; the change in geometry decreases the total load path and, correspondingly, the deflection.

A closer examination of the Pratt truss reveals that the diagonals carry the loads from the point of load application

to the reactions at the supports. The verticals do not carry the loads closer to the supports of the truss; can they, then, be replaced with a different layout? This observation prompts an examination of a Warren truss (Figure 5). In this type of truss, the tension load path is further reduced to $\sum F_T L_T = 8PB$, and the compression load path is reduced to $\sum F_C L_C = 7PB$. While the difference remains at PB , the total load path has been further reduced to $15PB$, and the corresponding deflection is reduced to $15\sigma B/E$. By changing the geometry of the structure, it is possible to reduce the volume of material and make it stiffer—a remarkable achievement.

Figure 6 shows a truss with a still shorter load path. It represents a minimum load path solution for a structure with a geometry bounded to a depth B and 12 members. Although it appears a bit unusual, the geometry is very regular with the intersection of all the tension and compression members happening at nearly the same angle. If the angles are made to be the same, the load path only increases 0.03%. For a span to depth ratio of 2.63:1, the angle between the tension and compression members will be 60 degrees, and the triangles become 30/60/90 right triangles. The solution in Figure 6 provides a benchmark for judging the efficiency of other geometries.

Minimum load path is not the only consideration in selecting a final solution. For example, the designer needs to consider issues such as complexity, cost, usability, aesthetics, multiple loading conditions and permitted stresses

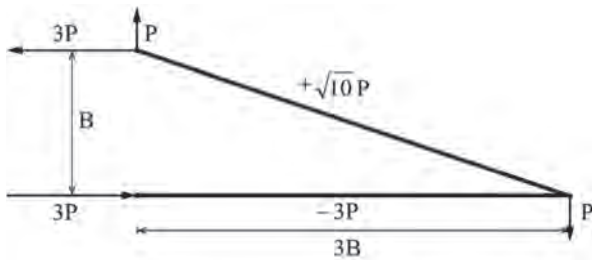


Fig. 3. Truss geometry selected for shortest path, which coincides with the moment diagram.

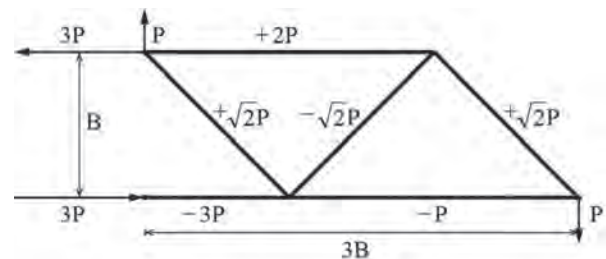


Fig. 5. Geometry of a Warren truss.

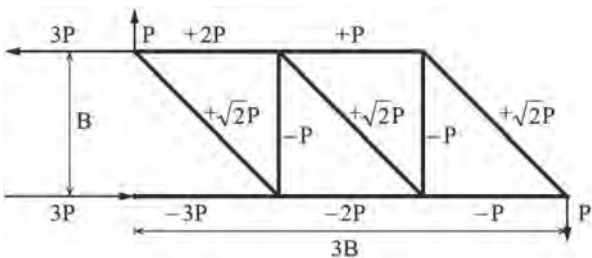


Fig. 4. Geometry of a Pratt truss.

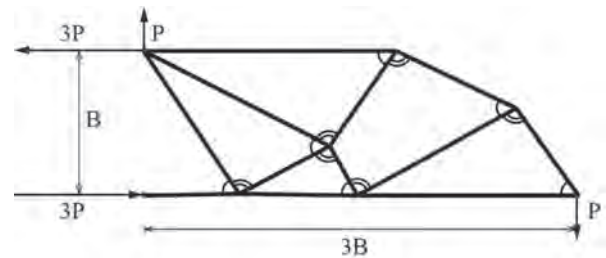


Fig. 6. Bounded optimal truss with 12 members.

Table 1. Load Path and Deflection Comparisons for 3:1 Cantilever					
	Tensile Load Path, $\sum F_T L_T$	Compressive Load Path, $\sum F_C L_C$	Difference in Load Paths, $\sum F_T L_T - \sum F_C L_C$	Sum of Load Paths, $\sum F_T L_T + \sum F_C L_C$	Deflection, Δ
Moment diagram truss	10PB	9PB	PB	19PB	$19 \frac{\sigma B}{E}$
Pratt truss	9PB	8PB	PB	17PB	$17 \frac{\sigma B}{E}$
Warren truss	8PB	7PB	PB	15PB	$15 \frac{\sigma B}{E}$
Bounded optimal truss	7.7PB	6.7PB	PB	14.47PB	$14.47 \frac{\sigma B}{E}$
Compression chord cantilever	8.52PB	7.52PB	PB	16.04PB	$16.04 \frac{\sigma B}{E}$

for tension and compression. For example, if the designer decides to limit the number of compression members to a minimum, Figure 7 provides a solution. Once again, this structure is very regular, with all the tension members from the support intersecting the compression chord at the same angle. A comparison to the geometry in Figure 6 shows that the Figure 7 geometry has a load path that is 10.9% larger.

A comparison of these geometries is provided in Table 1. It is advised that the reader study the relationships among the internal forces, total load paths and deflections to develop his or her own insight into the problem.

Deflections are often an important consideration in the design of structures. If a structure is uniformly stressed, the relative volume of steel needed by alternate truss geometries to achieve a target deflection can be shown equal to the square of the ratio of the load paths. This can be shown as follows.

If the volumes of any two structures in Table 1 are compared with one another, we have:

$$V_1 = \frac{\alpha_1 PB}{\sigma_1} \quad (3)$$

and

$$V_2 = \frac{\alpha_2 PB}{\sigma_2} \quad (4)$$

where α represents the coefficient of the sum of the load paths in Table 1. Because the deflection is set to be equal,

$$\Delta = \alpha_1 \sigma_1 \frac{B}{E} = \alpha_2 \sigma_2 \frac{B}{E} \Rightarrow \sigma_2 = \frac{\alpha_1}{\alpha_2} \sigma_1 \quad (5)$$

Thus, the ratio of the volumes can be computed as

$$\frac{V_2}{V_1} = \frac{\alpha_2^2 PB}{\alpha_1 PB} = \left(\frac{\alpha_2}{\alpha_1} \right)^2 \quad (6)$$

This example shows that load path is a major consideration in the efficiency of deflection-controlled designs. For example, the Pratt truss in Table 1 needs 28% more tonnage to achieve the same deflection as the Warren truss or 38% more material than the Bounded Optimal truss with 12 members.

The preceding examples certainly beg the question: How low can one go? The geometry of the lowest unbounded load path structure and the magnitude of its load path have been studied in the work of Mazurek and colleagues (2011; 2012) (see Figure 8). This research shows that the structure of minimal load path has a value of approximately $\sum F_T L_T + \sum F_C L_C = 13.17PB$. Once again, all the tension

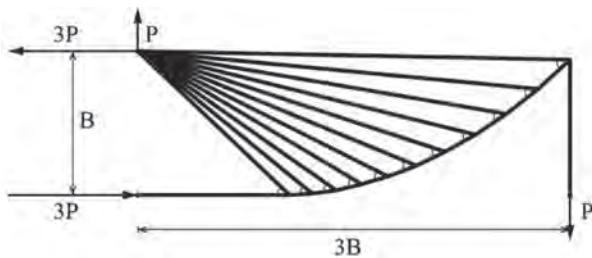


Fig. 7. Cantilever with only compression chord.

members intersect the compression members at the same angle. Although a structure in Figure 8 would generally be deemed impractical, it does provide a benchmark for judging alternate solutions. This will be discussed further in a later section.

AN APPLICATION OF MAXWELL'S THEOREM

For structures in which the external loads do not change as the geometry changes (generally simply supported structures), the dot product of the external forces and an arbitrarily selected origin will be a constant. Using this constant, Maxwell's theorem can determine the entire load path of a structure by calculating the constant and either the compression or tension load paths. The total load path is equal to twice the tension load path minus the constant or twice the compression load path plus the constant.

For example, consider Exchange House in London for which the first author (Baker) led the structural engineering team in the 1980s (Figure 9). This is a 10-story office building that spans over a series of rail lines and is supported by four 7-story parabolic arches. The author was not aware of Maxwell's load path theorem at the time of the design, so the geometry was developed using labor-intensive parametric studies. These parametric studies can be replaced by a simple application of Maxwell's theorem.

It can be inferred from Maxwell's theorem that if the tension load path is minimized, the total load path will also be

minimized. To simplify calculations, the parameters B , H and W are used to describe the span and height of the building and the width tributary to an arch; z denotes the depth of the arch; and γ is the average density (weight including live load) of the building. In what follows, the columns and hangers will be simplified by considering them as a continuum.

The tension load path can be readily calculated, as shown in Figure 10. The force in the tie is equal to the overall moment in the system divided by the depth of the arch, $\gamma W H B^2 / 8z$; the length of the tie is equal to the width of the building, B . The total load path for the tie is $\gamma W H B^3 / 8z$. The load path of the hangers in Figure 10 can also be calculated as follows:

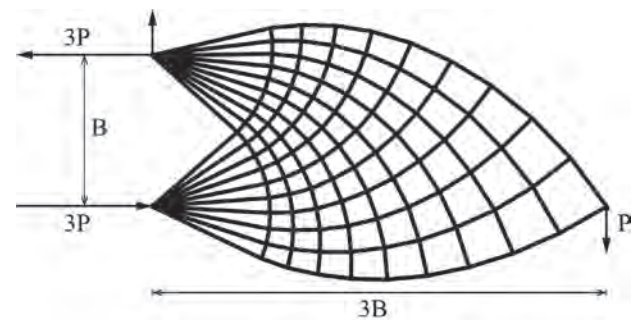


Fig. 8. Optimal geometry for 3:1 cantilever based on the three-point load solution.



Fig. 9. Exchange House in London.

$$\sum_{\text{hangers}} F_T L_T = 2 \int_0^{B/2} \int_0^z \left(1 - \left(\frac{2x}{B}\right)^2\right) \gamma W y \, dy \, dx = \frac{4}{15} \gamma W B z^2 \quad (7)$$

Thus, the total tension load path is the sum of the tie and the hangers:

$$\sum F_T L_T = \sum_{\text{hangers}} F_T L_T + \sum_{\text{tie}} F_T L_T = \frac{4}{15} \gamma W B z^2 + \frac{\gamma W B^3 H}{8z} \quad (8)$$

The depth of the arch that will minimize the total load path of the structure (tension and compression load paths) can be found by taking a simple derivative of Equation 8:

$$\frac{d\left(\sum F_T L_T\right)}{dz} = 0 \Rightarrow \frac{8Bz}{15} - \frac{B^3 H}{8z^2} = 0 \Rightarrow z = \sqrt[3]{\frac{15B^2 H}{64}} \quad (9)$$

How does this result, based on a continuum, compare to the discrete problem with a finite number of columns and floors? Although not presented here, the authors have compared the results from Equations 8 and 9 to a calculation based on the discrete members of the Exchange House project and have found that the results are within 2%.

It should also be noted that the actual height of the Exchange House arch is lower than the optimum height because of a design requirement to find a close match of the parabolic arch to the grid of the columns and floors. The premium of the lower arch was deemed appropriate for the resulting simplicity of the connections, location of work-points, etc.

Maxwell's theorem can also be used to calculate the total load path of the structure. For this structure, the dot product, $\sum \bar{P}_i \cdot \bar{r}_i$, is a constant that is very easily calculated; it is equal to the load path that would exist if the building sat on the ground and was only supported by columns (Figure 11).

$$\begin{aligned} \sum \bar{P} \cdot \bar{r} &= -\gamma B H W \cdot \frac{H}{2} \\ &= -\frac{\gamma B H^2 W}{2} \end{aligned} \quad (10)$$

Using twice the tension load path minus the constant, the total load path of the structure can be calculated as follows:

$$\begin{aligned} \sum_{\text{total}} FL &= 2 \left(\sum F_T L_T \right) - \sum \bar{P} \cdot \bar{r} \\ &= 2 \left(\frac{4}{15} \gamma W B z^2 + \frac{\gamma W B^3 H}{8z} \right) - \left(-\frac{\gamma W B H^2}{2} \right) \\ &= \gamma B H W \left[\frac{8}{15} \frac{z^2}{H} + \frac{B^2}{4z} + \frac{H}{2} \right] \end{aligned} \quad (11)$$

The total steel tonnage of the structure can now be estimated. For a structure of this scale, it is not unusual for the permitted tensile and compressive stresses for steel to be very similar. The tension members are controlled by the net-section issues; the compression members are controlled by buckling capacity. Dividing the total load path by an estimated average stress, σ , will provide an estimated total tonnage of steel.

Hopefully, this example helps the reader appreciate the power of Maxwell's theorem. The theorem enables the optimization for the conceptual design of a large structure and an estimate of the total tonnage of steel in a few short calculations without actually sizing a single member.

It is worth reflecting that the preceding process calculated the load path in the arch without directly calculating the forces in the arch. How is this possible? It is instructive to examine Figure 12. The load path in a diagonal member (such as a segment of an arch) is equal to the vertical component of the force times the vertical dimension of the member plus the horizontal component of the force times the horizontal dimension of the member. Using this knowledge, the following analysis shows how the arch load path is implicitly included.

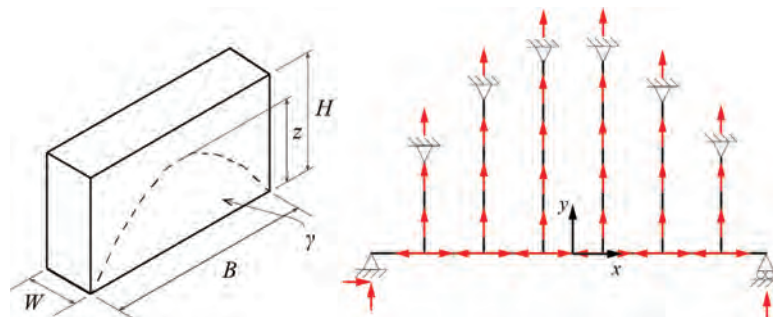


Fig. 10. Schematic of the building dimensions and tension members (tie and hangers) for Exchange House.

For the total structure (Figure 13), from Maxwell's theorem, it can be shown that

$$\sum_{total} FL = 2 \sum_{tie} F_T L_T + 2 \sum_{hangers} F_T L_T - \sum \vec{P} \cdot \vec{r} \quad (12)$$

This must also be equal to

$$\sum_{total} FL = \sum_{tie} F_T L_T + \sum_{hangers} F_T L_T + \sum_{columns\ above\ arch} F_C L_C + \sum_{arch} F_C L_C \quad (13)$$

The dot product in Equation 12 can be split into two values: the load path above the arch and the load path below the arch, as if the structure was supported directly on the ground:

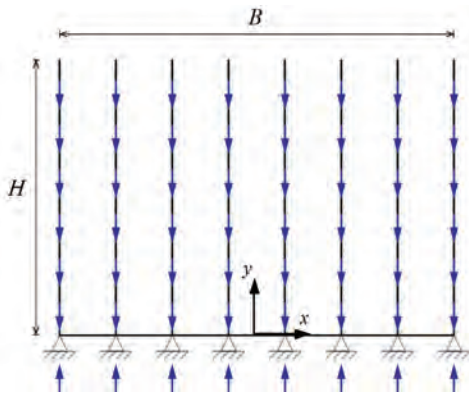


Fig. 11. Schematic for Exchange House with column support only.

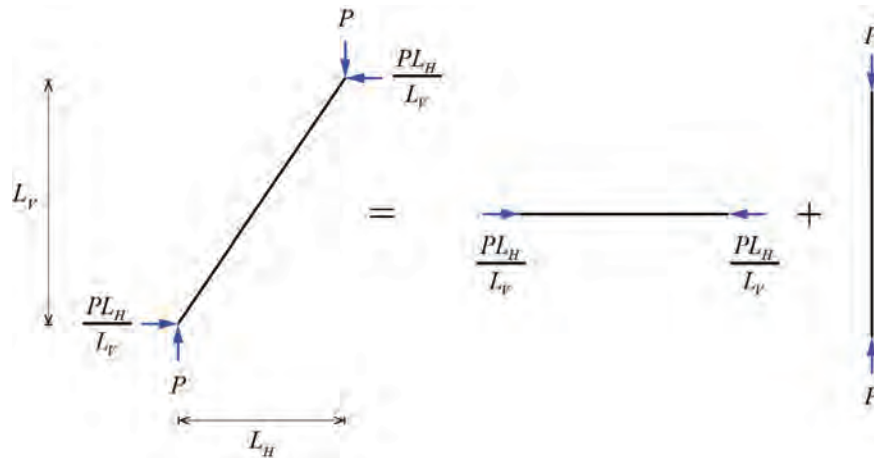


Fig. 12. Segment of an arch decomposed into a horizontal and vertical component.

$$\sum \vec{P} \cdot \vec{r} = - \sum_{columns\ above\ arch} F_C L_C - \sum_{columns\ below\ arch} F_C L_C \quad (14)$$

Therefore, substituting into the total load path equation, the load path of the arch is simply

$$\sum_{arch} F_C L_C = \sum_{tie} F_T L_T + \sum_{hangers} F_T L_T + \sum_{columns\ below\ arch} F_C L_C \quad (15)$$

which is shown graphically in Figure 14.

Here, we can see that the horizontal load path of the arch is equal to the horizontal load path of the adjacent tie plus the vertical load paths of the adjacent hangers plus the vertical load paths of the columns that were eliminated when the arch system was used instead of sitting directly on the ground. This is a remarkably sophisticated result from Maxwell's very simple equation.

MICHELL TRUSSES

In 1904, A.G.M. Michell wrote a seminal paper in which he outlined the principles of trusses with the shortest possible load paths and presented a limited number of solutions. Michell started with Maxwell's load path theorem and concluded that, if a continuous orthogonal deformation field is produced where all the tension elements are equally strained (elongated) and all the compression elements experience the same strain but are compressed, then the structure defined by these strain fields will be minimal, with the total load path of the structure equal to the work done by the external forces moving in this assumed displacement field. These displacement fields must satisfy certain mathematical relations and result in orthogonal tension and compression strain fields. It should be noted that the mathematics of these strain

fields are related to the slip lines in the Theory of Plasticity.

Discussed next are some of the truss geometries of minimal load path structures included in Michell's 1904 paper (see Figure 15). Because Michell approached the problem from the point-of-view of continuum mechanics, it should be noted that the following solutions permit an infinite number of elements (only a few of the members are drawn in the bicycle wheel like structures or the equilateral spirals of Figure 15). Nevertheless, Michell trusses are quite useful because they provide insight into optimal geometries and are benchmarks of the shortest possible load path for a

given structure. In the design of practical trusses, however, the final structures are composed of a finite number of elements. Thus, it is useful to look at the discretized versions of these optimal solutions, commonly referred to as discrete Michell trusses or discrete optimal trusses.

DISCRETE OPTIMAL TRUSSES

Research on discrete Michell trusses has produced results that are also useful in understanding optimal load path structures. Though these discrete Michell truss structures

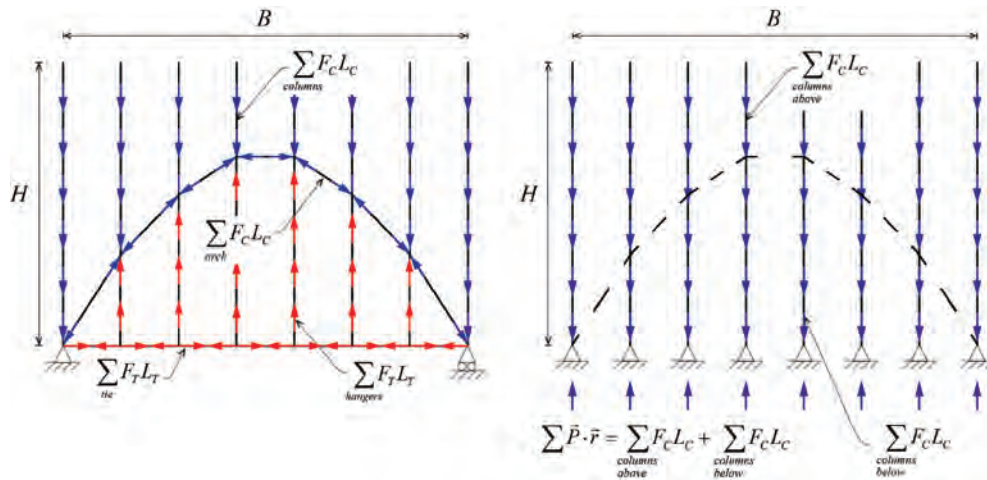


Fig. 13. Total load path of Exchange House.

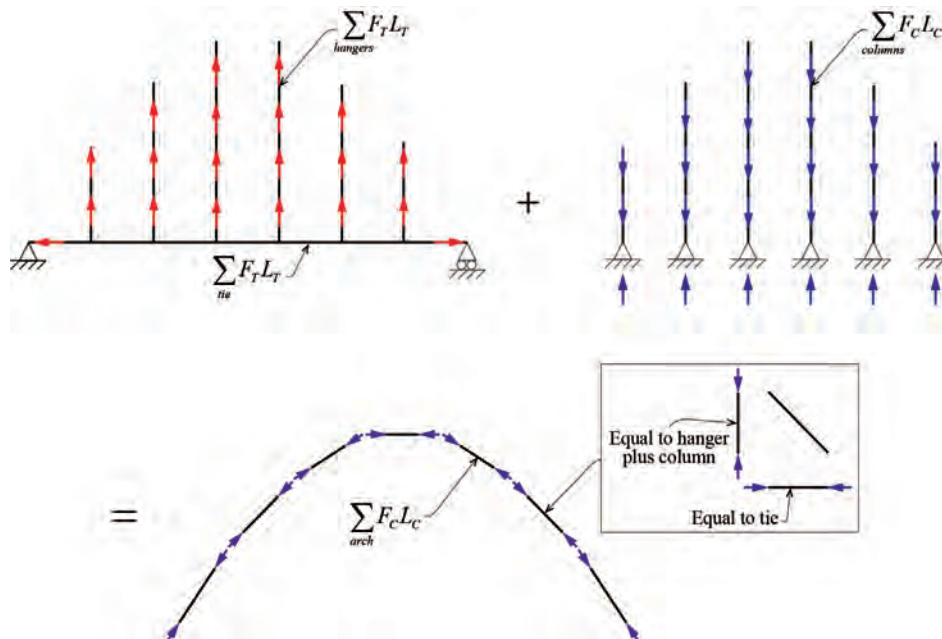


Fig. 14. Calculation of load path of the arch for Exchange House

are often impractical to build, they provide excellent benchmarks for designers in terms of efficiently utilizing materials. Recent work by Mazurek and colleagues (2011; 2012) and has shown that these discrete trusses can have amazing regularity and order. In the class of problems in which there is a symmetrical cantilever with two points of support and a single load, the complete geometry can be described using only one angle (denoted by α in Figure 16); the adjacent angles are right angles or complements of the first angle. An example can be seen in Figure 16, which was also studied by Chan (1960).

It is interesting to note that the optimal structure for the discrete Michell cantilever in Figure 16 is composed of several substructures, each of which is also optimal for the given number of members and connectivity. For example, the optimal geometry for a structure of two members is shown in the substructure, ξ_2 , of Figure 16. Likewise, for eight members, the optimal structure is embedded in the larger optimal structures, composed of 18, 32, 50 and so on members. For a complete set of graphical rules to construct such geometries for three-point or three-force structures, the reader is referred to Mazurek and colleagues (2011; 2012).

The exact derivation of the optimal geometry for discrete trusses using Michell's theories or graphical rules, such as those shown by Mazurek and colleagues (2011), is often quite difficult for complicated loadings. Fortunately, today, designers have some powerful tools to assist in approximating optimal topologies for these more complex structures. Several of these tools include topology optimization using material distribution methods, such as the SIMP (Solid Isotropic Material with Penalization) material model (Bendsoe and Sigmund, 2002; Rozvany, Zhou and Birker, 1992), or discrete truss topology optimization methods based on ground structures (see Chapter 4 of Bendsoe and Sigmund, 2002, or Chapter 5 of Christensen and Klarbring, 2009). A brief overview of these tools is given in the following section.

TOPOLOGY OPTIMIZATION APPROACHES

According to Bendsoe and Sigmund (2002), topology optimization consists of studying the optimal arrangement of isotropic material in space for the design of the topology of a structure. A geometric representation of such a structure can be thought of as a black-and-white rendering of an image, in which the "pixels" are given by finite elements. This methodology essentially starts with a uniformly distributed "gray" material in which the optimal layout is determined through an iterative process to reveal a potentially optimal load path, represented by "black" and "white" densities. An example of this methodology can be seen in Figure 17 using the educational codes provided in Talischi and colleagues (2012a; 2012b) for the topology optimization of a 6:1 simple span problem with five sets of uniformly spaced point loads. One of the major advantages of this methodology is that the feasible solutions can have any size, shape or connectivity. For an example of the use of topology optimization in the design of steel bracing systems of high-rise buildings, refer to Stromberg and colleagues (2012).

An alternative approach based on ground structures considers a form of gridlike continua for the topology optimization of trusses using discrete members; this can also be viewed as a sizing problem where the connectivity must be specified *a priori*. Within these techniques, there are literally thousands of interconnected truss elements that coalesce into patterns based on the final optimal cross-sectional areas that reveal optimal (minimal) load path structures. To generate such topologies using this approach, refer to the educational code provided in Sokol (2011); see Figure 18.

The interpretation of the results computed using either of these tools requires a significant amount of engineering judgment and an understanding of practical issues such as constructability and functionality of the truss. Using these solutions, a discrete truss, which provides the general connectivity of the structure, can be interpreted. However, the

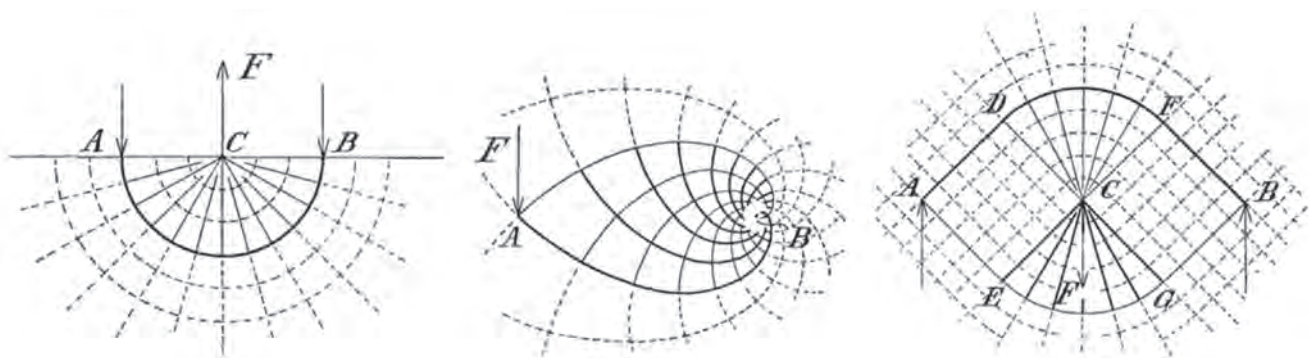


Fig. 15. Minimal load path structures taken from Michell (1904): semi-infinite fan (left), orthogonal systems of equiangular spirals (center) and centrally loaded beam (right).

determination of the precise location of the joints (nodes) can be quite subjective because it is often an “eyeball” estimate of the location. Therefore, after the connectivity is identified, the final “optimal” locations of the nodes might then be refined using various searching or gradient optimization techniques. One useful method that also gives great insight into the forces in the individual members is Graphic Statics.

GRAPHIC STATICS

Graphic Statics is a powerful tool for studying both the geometry and the forces in a structure using only graphical methods. It was once in wide usage, initially based on the work of Rankine and Maxwell and later adopted and refined by Culmann and Cremona. Graphic Statics has recently been revived in the design of compression-only masonry shells in the work of Block and Ochsendorf (2007).

Graphic Statics uses graphical techniques to determine the axial forces in certain common trusses geometries. It was originally done with simple drafting tools and can now be easily done with computer graphic programs or simple spreadsheets. It does not require the calculation of stiffness,

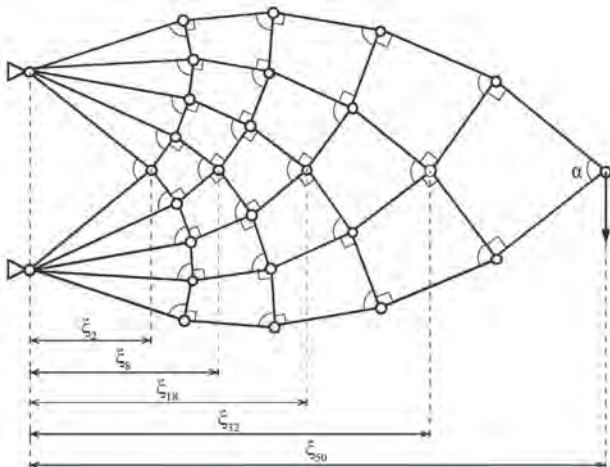


Fig. 16. Optimal discrete Michell truss.

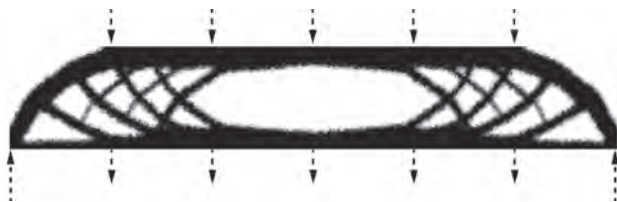


Fig. 17. Topology optimization approach by distribution of isotropic material using the educational code, PolyTop (Talischi et al., 2012a; 2012b).

only simple geometrical relationships. It produces two diagrams—one that represents the geometry of the truss and the other that represents the axial forces in the members of the truss. Maxwell determined that these two diagrams are reciprocal.

Cremona later modified this concept so that, for each line in the form diagram (truss geometry), there is a parallel line in the force diagram, the length of which is proportional to axial force in the original form line (truss member). Maxwell also determined that each node in the form diagram maps into a closed polygon in the force diagram, which represents the equilibrium of the forces at the node. Also, every polygon in the form diagram maps into a node in the force diagram. Because these two diagrams are reciprocal, the mapping can also be reversed. This means that the designer can manipulate the force diagram in order to determine the geometry that produces a desired set of forces.

As described by Baker and colleagues (2013), for a given connectivity of nodes, Graphic Statics provides all the information needed to determine the total load path of the structure in the form and force diagrams; that is, using the form diagram, the member lengths can be found while the force diagram provides the corresponding member forces. Thus, all of the information is graphically available to determine the total load path.

To understand the mappings between the reciprocal diagrams, consider the simple six-panel gable truss (Zalewski and Allen, 1998) shown in Figure 19. On the left, the geometry of the structure, or the form diagram, is shown. The lines in the form diagram represent structural members or, rather, lines of action of the structural members. The lines in the second diagram (on the right of Figure 19), known as the force diagram, represent forces carried by the members from the form diagram. In this figure, dashed line vectors are used to represent these external forces both in the form and force diagrams.

The notation used in Figure 19 and following diagrams is an interval notation based on a version of Bow’s notation (Bow, 1873). For the form diagram, the capital letters, A, B, C, ... , are sequentially placed clockwise in the intervals between external forces (open polygons) and numbers, 1, 2, 3, ... , are placed in the internal spaces (closed polygons)

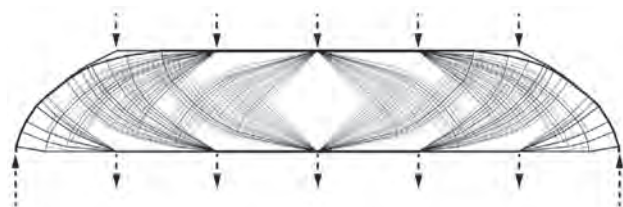


Fig. 18. Topology optimization approach using ground structures, computed by the educational code in Sokol (2011).

between members. Each line in the form diagram is bordered by two polygons. Thus, a member may be referred to using the corresponding letter or number of the adjacent polygons—for example, A-1 or 2-3—and a joint called with a series of letters and numbers—for example, A-B-3-2-1-A. Similarly, the external forces are referenced using the adjacent open polygons—for example, F_{AB} . The open polygons denoted by capital letters in the form diagram correspond to points (nodes) on the load line of the force diagram, denoted by the lowercase letters, a, b, c, \dots . The numbers denoting the closed polygons in the form diagram also have corresponding nodes in the force diagram.

This graphical methodology allows the user to determine the axial force in a truss member by measuring the length of the reciprocal line in the force diagram. The relative magnitude of the force diagram is set by drawing the load line, which represents the external forces, to scale. For example, the force in member A-1 in the form diagram of Figure 18 is proportional to the length of the line between points a and 1 in the corresponding force diagram. Similarly, the force in the member between polygons 2 and 3 is proportional to the length of the line between points 2 and 3 of the force diagram. The remaining forces in the other members can be computed likewise. It should be noted that nodes 1 and 2 overlay each other in the force diagram; this indicates that member 1-2 has zero force (the same is true for member 9-10). Thus, the forces acting on a node in the form diagram correspond to a polygon in the force diagram, where each force is a side of the polygon. For example, at node A-B-3-2-1-A, the polygon of forces is given by points $a-b-3-2-1-a$. Reading clockwise around joint A-B-3-2-1-A in the form diagram, we can determine if members A-1 and 2-3 are in tension or compression. If read from 1 to a on polygon $a-b-3-2-1-a$, we move from the lower left to the upper right, toward the joint A-B-3-2-1-A of the form diagram. Thus, member A-1 is in compression. Likewise, moving from 3 to 2 on the force polygon goes from the lower right to the upper left, or

toward the joint in the form diagram, so member 3-2 is also in compression. For more details on reciprocal relationships, refer to Baker and colleagues (2013) and Zalewski and Allen (1998).

A useful application of Graphic Statics for structural design has also been described in Chapter 14 of the book by Zalewski and Allen (1998) for form-finding of trusses by graphically solving for the nodal locations that give a constant chord-force truss. For example, the gable truss of Figure 19 is revisited in Figure 20, in which the objective becomes to find the geometry of a truss in which the force in the top chord is constant. This can be accomplished by manipulating the force diagram so that the lengths of lines $a-1, b-3, c-5, d-6, e-8$ and $f-10$ are the same, representing equal forces. After the force diagram is modified to achieve the desired properties, work backward to find the reciprocal form diagram, resulting in the desired geometry. This has been applied in the design of the structure by Robert Maillart shown in Figure 21. Note that the forces in members 2-3, 4-5, 6-7 and 8-9 are zero because the nodes are overlaid in the force diagram on the right. These members were eliminated from Maillart's structure.

Similarly, to find the geometry of the truss in which there is a constant force in both the top and bottom chords, the force diagram can be modified accordingly so that all lines in the force diagram corresponding to the members in the chords have the same length. This example can be seen in Figure 22.

The authors note that the force polygon and form diagrams can be manipulated in this figure to achieve higher or lower forces and shallower or deeper trusses, depending on the needs of the designer. Also, members 2-3, 4-5, 6-7 and 8-9 are all zero force members. They may still be required for considerations of stability or unbalanced loads, unless the chords have sufficient flexural strength and stiffness to address these issues.

As previously mentioned, an interpretation of topology

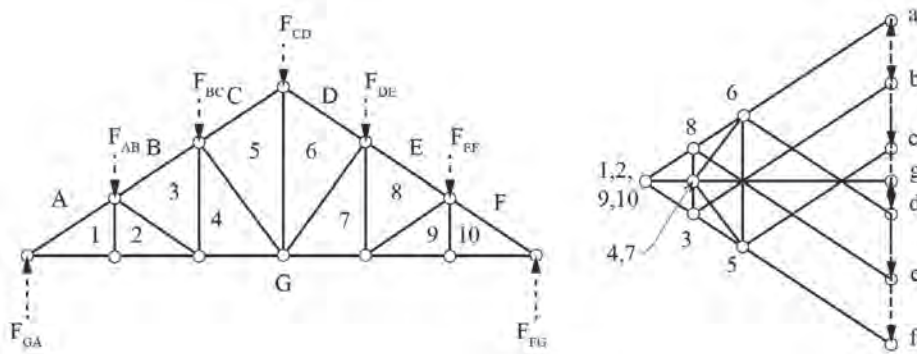


Fig. 19. Form and force diagrams for gable truss.

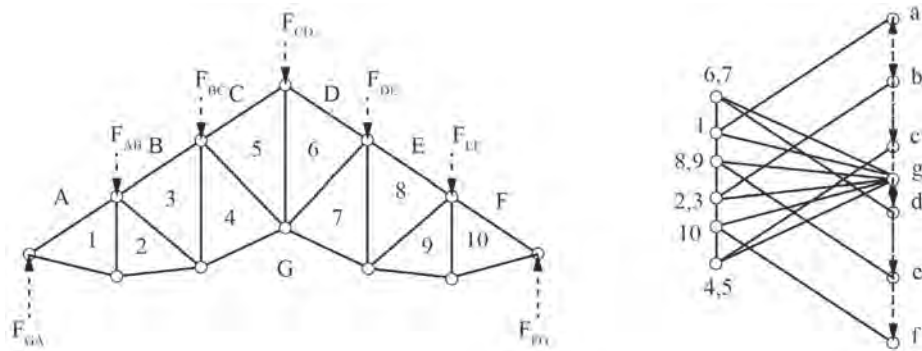


Fig. 20. Constant force gable truss (force is constant in top chord).



Fig. 21. Design using form-finding of a constant-force gable truss (Zalewski and Allen, 1998).

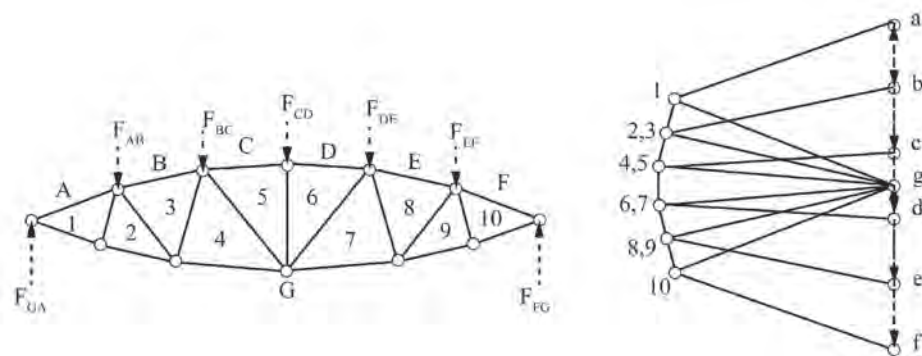


Fig. 22. Truss designed for constant and equal force in top and bottom chord.

optimization solutions from continuum or ground structure approaches provides approximate nodal locations and connectivity. Refinement of the nodal locations can be achieved through manipulation of the force diagram in graphic statics.

Figures 17 and 18 show the results of a continuum topology optimization by means of material distribution and ground structures, respectively. These results were then interpreted into general truss configurations, which give the general connectivity of nodes. To find a more precise location of nodes, various optimization techniques can be used. One method is to manipulate the force diagram of a graphic statics analysis until a minimum total load path is achieved. The reason the force diagram is manipulated rather than the form diagram is because we can always be assured that the solution is in equilibrium because the force polygons will always close. It can also be noted that because the solution is automatically constrained to be in equilibrium, there are fewer independent variables than if we tried to manipulate the form diagram. The result of this exercise is shown as truss A in Table 2. These solutions provide benchmarks against which the other truss geometries in Table 2 can be compared. It is worth noting that the geometry has a substantial influence on the potential efficiency of a truss, particularly when the design is deflection controlled. The geometry of the discrete optimal truss (truss A) is not common but is extremely regular, with the tension members intersecting the compression members at consistent angles.

The structural volume comparisons in Table 2 are appropriate for situations in which the permissible tensile and compressive stresses are similar in magnitude. The Warren truss, the combined Warren/Pratt truss and the compression diagonal Pratt truss (trusses C, D and E, respectively) have relatively short load paths and are appropriate for heavy trusses with stocky web members. They also have the advantage of having compression connections for the web members with the largest forces. Compression connections are often more efficient than tension connections for large forces.

The ranking of the truss geometries would change if the permitted compressive stresses were sensitive to the unbraced lengths. Trusses A and B would still have relatively low volumes because of the reduced unbraced lengths of the web members. To take full advantage of these geometries, designers need to consider the stabilizing effects of the tension diagonals and the benefits of connection continuity when determining the capacity of the compression diagonals in trusses A and B. These effects greatly increase the in-plane and out-of-plane buckling strength of the compression diagonals; the AISC direct analysis method is a good approach for capturing this benefit. Using this method,

the effective length factor K can be set equal to 1.0 for all the members, and by considering a second-order numerical analysis with modified members' stiffness, it is possible to capture the increased strength in the members.

The Pratt truss with tension diagonals (truss F) is often an appropriate geometry for trusses with slender members where the permitted compressive stresses are very sensitive to unbraced length. In such situations, truss F may have less tonnage than the trusses with compression diagonals. Truss F also benefits from fewer connections than trusses A and B and may be easier to erect than trusses with compression diagonal at the support. When considering a geometry similar to truss F, the designer should understand that the truss has a fundamentally longer total load path; some of the savings in web members will be offset with additional forces in chords and web members, as well as increased deflections. These "hidden" penalties are often overlooked when the designer only studies the web members when determining the geometry of a truss.

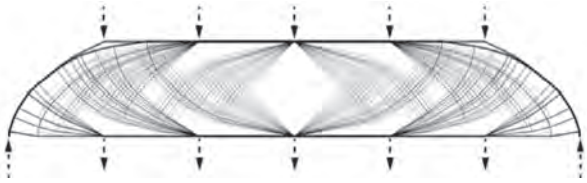
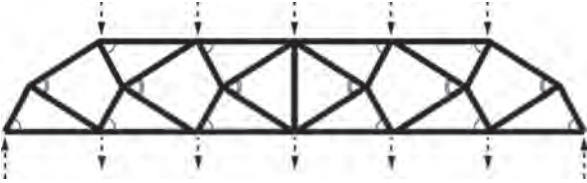
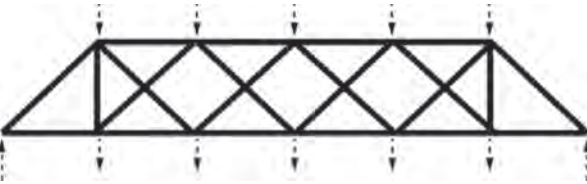
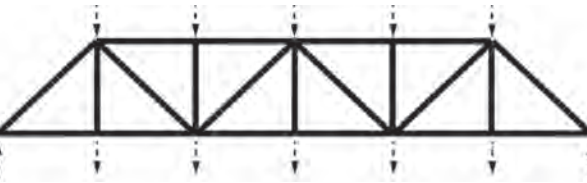
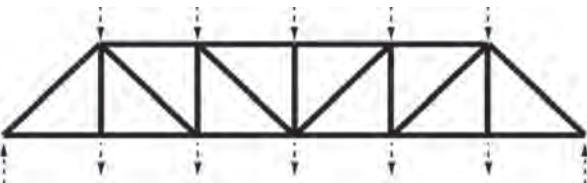
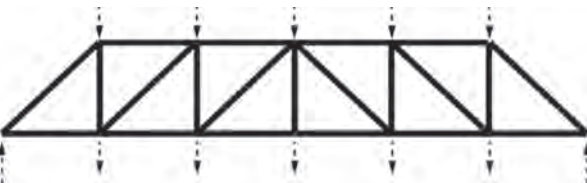
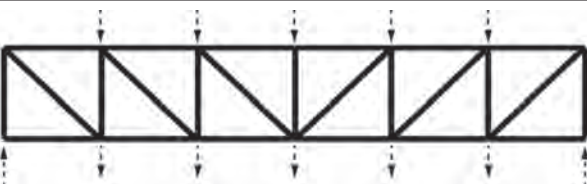
CONCLUSIONS

Several years ago, the first author (Baker) heard a reference to Michell trusses while attending an overseas conference. An attempt to learn more about the subject prompted the purchase of an out-of-print book that included Michell's 1904 paper. The work was both illuminating and thought-provoking. Exploration of Michell's work led the authors to Maxwell. Unfortunately, while Maxwell produced an immense body of work, much of it is unrelated to structural engineering. Seeking a guide to Maxwell, the authors turned to the *History of Strength of Materials* by Timoshenko (1953). This inquiry into Maxwell ultimately led the authors to Rankine, Cremona and a reexamination of Airy. Amazingly, several of their important ideas are no longer common currency (or may have never been widely known). The search for lost ideas continues.

Maxwell's load path theorem is simple and powerful. Inefficiencies must be paid for twice—once in tension and once in compression. Minimize one and the other is also minimized. Michell trusses provide benchmarks for least load path solutions. Discrete Michell trusses are amazingly regular and ordered; their shapes both surprising and informative. While Graphic Statics has been replaced by the computer as an analysis tool, it remains a powerful design tool. Modern topology optimization tools make finding efficient layouts for complex problems accessible to the designer. The authors have found that these ideas and tools greatly aid in the conceptual design of trusses and other structures.

The working title for this paper was "things I wish I had

Table 2. Relative Efficiency of Various Trusses Compared to Minimum Load Path Structures

Discretized Solution	Volume Ratio for Constant Stress	Deflection for Constant Stress	Volume Ratio for Equal Deflection
 <p data-bbox="376 534 662 562">Ground structures solution</p>	100%	100%	100%
 <p data-bbox="343 761 695 789">Truss A: Discretized optimal truss</p>	102.6%	102.6%	105.3%
 <p data-bbox="409 987 629 1015">Truss B: Lattice truss</p>	111.6%	111.6%	124.7%
 <p data-bbox="409 1213 629 1241">Truss C: Warren truss</p>	111.6%	111.6%	124.7%
 <p data-bbox="327 1440 712 1468">Truss D: Combined Warren/Pratt truss</p>	113.7%	113.7%	129.2%
 <p data-bbox="294 1666 745 1694">Truss E: Compression diagonal Pratt truss</p>	119.7%	119.7%	143.3%
 <p data-bbox="327 1892 712 1920">Truss F: Tension diagonal Pratt truss</p>	129.8%	129.8%	168.4%

known when I started designing structures.” None of the preceding theorems, tools or techniques was included in the authors’ engineering education, but all are useful in developing an efficient structural design. Quite simply, the potential efficiencies or inefficiencies of a design are determined by the structural geometry. No amount of optimizing the size of individual members will compensate for a bad structural layout. The authors hope that the paper makes this information available to today’s structural engineering educators and practicing structural engineers so that they can create efficient designs that conserve our resources and reduce the carbon footprint of our construction.

ACKNOWLEDGMENTS

The authors wish to acknowledge the contributions of the following individuals to the work discussed in this paper: Glaucio H. Paulino, Cenk Tort, Neil Katz and Joshua Schultz. Particular appreciation is extended to Beth Murin for editing the text.

REFERENCES*

- Airy, G.B. (1863), “On the Strains in the Interior of Beams,” *Philosophical Transactions of the Royal Society of London*, Vol. 153, pp. 49–71.
- Baker, W.F., Beghini, L.L., Mazurek, A., Carrion, J. and Beghini, A. (2013), “Maxwell’s Reciprocal Diagrams and Discrete Michell Frames,” *Structural and Multidisciplinary Optimization*, Vol. 48, Issue 2, pp. 267–277.
- Beghini, A., Beghini, L.L., Schultz, J.A., Carrion, J. and Baker, W.F. (2013), “Rankine’s Theorem for the Design of Cable Structures,” *Structural and Multidisciplinary Optimization*, Vol. 48, Issue 5, pp. 877–892.
- Bendsoe, M.P. and Sigmund, O. (2002), *Topology Optimization: Theory, Methods and Applications*, Springer, Berlin.
- Block, P. and Ochsendorf, J. (2007), “Thrust Network Analysis: A New Methodology for Three-Dimensional Equilibrium,” *Journal of the International Association for Shell and Spatial Structures*, Vol. 48, No. 3, pp. 1–8.
- Bow, R.H. (1873), *Economics of Construction in Relation to Framed Structures*, ICE Publishing, London.
- Chan, A.S.L. (1960), “The Design of Michell Optimum Structures,” Ministry of Aviation Aeronautical Research Council Report, No. 3303, pp. 1–40.
- Christensen, P.W. and Klarbring, A. (2009), *An Introduction to Structural Optimization*. Springer.
- Cox, H.L. (1965), *The Design of Structures of Least Weight*, Pergamon Press, Oxford, United Kingdom.
- Forfar, D.O. (2012), “Maxwell, Einstein, Newton and Faraday,” *Newsletter of the James Clerk Maxwell Foundation*, Vol. 1, p. 2.
- Maxwell, J.C. (1864), “On Reciprocal Figures and Diagrams of Forces,” *Philosophical Magazine*, Vol. 26, pp. 250–261.
- Maxwell, J.C. (1870), “On Reciprocal Figures, Frames, and Diagrams of Forces,” *Edinbrook Royal Society Proceedings*, Vol. 7, pp. 160–208.
- Mazurek A. (2012). “Geometrical Aspects of Optimum Truss-Like Structures for Three-Force Problem,” *Structural and Multidisciplinary Optimization*, Vol. 45, No. 1, pp. 21–32.
- Mazurek, A., Baker, W.F. and Tort, C. (2011), “Geometrical Aspects of Optimum Truss-Like Structures,” *Structural and Multidisciplinary Optimization*, Vol. 43, No. 2, pp. 231–242.
- Michell, A.G.M. (1904), “The Limits of Economy of Material in Frame-Structures,” *Philosophical Magazine*, Vol. 8, No. 47, pp. 589–597.
- Rozvany, G.I.N., Zhou, M. and Birker, T. (1992), “Generalized Shape Optimization without Homogenization,” *Structural and Multidisciplinary Optimization*, Vol. 4, No. 3, pp. 250–252.
- Sokol, T. (2011), “A 99 Line Code for Discretized Michell Truss Optimization Written in Mathematica,” *Structural and Multidisciplinary Optimization*, Vol. 43, pp. 181–190.
- Stromberg, L.L., Beghini, A., Baker, W.F. and Paulino, G.H. (2012), “Topology Optimization for Braced Frames: Combining Continuum and Beam/Column Elements,” *Engineering Structures*, Vol. 37, pp. 106–124.
- Talischi, C., Paulino, G.H., Pereira, A., and Menezes, I.M.F. (2012a), “PolyMesher: A General-Purpose Mesh Generator for Polygonal Elements Written in Matlab,” *Structural and Multidisciplinary Optimization*, Vol. 45, No. 3, pp. 309–328.
- Talischi, C., Paulino, G.H., Pereira, A., and Menezes, I.M.F. (2012b), “PolyTop: A Matlab Implementation of a General Topology Optimization Framework Using Unstructured Polygonal Finite Element Meshes,” *Structural and Multidisciplinary Optimization*, Vol. 45, No. 3, pp. 329–357.
- Timoshenko, S.P. (1953), *History of Strength of Materials*. McGraw-Hill Book Company, New York.
- Zalewski, W. and Allen, E. (1998), *Shaping Structures: Statics*. John Wiley & Sons, New York.

* Many of the older references are within the public domain and can be downloaded from Google Books.

GUIDE FOR AUTHORS

SCOPE: The ENGINEERING JOURNAL is dedicated to the improvement and advancement of steel construction. Its pages are open to all who wish to report on new developments or techniques in steel design, research, the design and/or construction of new projects, steel fabrication methods, or new products of significance to the uses of steel in construction. Only original papers should be submitted.

GENERAL: Papers intended for publication may be submitted by mail to the Editor, Margaret A. Matthew, ENGINEERING JOURNAL, AMERICAN INSTITUTE OF STEEL CONSTRUCTION, One East Wacker Drive, Suite 700, Chicago, IL, 60601, or by email to matthew@aisc.org.

The articles published in the *Engineering Journal* undergo peer review before publication for (1) originality of contribution; (2) technical value to the steel construction community; (3) proper credit to others working in the same area; (4) prior publication of the material; and (5) justification of the conclusion based on the report.

All papers within the scope outlined above will be reviewed by engineers selected from among AISC, industry, design firms, and universities. The standard review process includes outside review by an average of three reviewers, who are experts in their respective technical area, and volunteers in the program. Papers not accepted will not be returned to the author. Published papers become the property of the American Institute of Steel Construction and are protected by appropriate copyrights. No proofs will be sent to authors. Each author receives three copies of the issue in which his contribution appears.

MANUSCRIPT PREPARATION: Manuscripts must be provided in Microsoft Word format. Include a PDF with your submittal. View our complete author guidelines at www.aisc.org/ej.



There's always a solution in steel.

ENGINEERING JOURNAL
American Institute of Steel Construction
One East Wacker Drive, Suite 700
Chicago, IL 60601

312.670.2400

www.aisc.org